

CLATHRIN LIGHT CHAIN DIVERSITY REGULATES LATTICE PROPERTIES AND EFFICIENCY OF SYNAPTIC VESICLE FORMATION

Lisa Redlingshöfer^{1,2}, Faye McLeod³, Marine D. Camus^{1,2}, Yu Chen^{1,2}, Jemima J. Burden⁴,
Ernest Palomer Vila³, Kit Briant^{1,2}, Philip N. Dannhauser^{1,2}, Patricia C. Salinas³ and Frances
M. Brodsky^{1,2*}

¹ Research Department of Structural and Molecular Biology, Division of Biosciences,
University College London, Gower Street, London WC1E 6BT, UK

² Institute of Structural and Molecular Biology, Birkbeck and University College London,
Malet Street, London WC1E 7HX, UK

³ Research Department of Cell and Developmental Biology, Division of Biosciences,
University College London, Gower Street, London WC1E 6BT, UK

⁴ Medical Research Council Laboratory for Molecular Cell Biology, University College
London, Gower Street, London WC1E 6BT, UK

*to whom correspondence should be addressed:

Professor Frances M. Brodsky

f.brodsky@ucl.ac.uk

ABSTRACT

Clathrin light chain (CLC) subunits in vertebrates are encoded by paralogous genes *CLTA* and *CLTB* and both gene products undergo alternative splicing in neurons. To understand how this CLC diversity influences neuronal clathrin function, we characterised the biophysical properties of clathrin comprising individual CLC variants for correlation with neuronal phenotypes of mice lacking either CLC-encoding gene. CLC variants differentially influenced clathrin knee conformation within assemblies, and clathrin lattices with neuronal CLC mixtures were more effective in membrane bending than those with single neuronal isoforms nCLCa or nCLCb. Correspondingly, electrophysiological recordings revealed that neurons from mice deficient for nCLCa or nCLCb were defective in synaptic vesicle recycling. Mice with only nCLCb had a reduced synaptic vesicle pool compared to wild-type mice, while nCLCa-only mice had increased synaptic vesicle numbers. These findings highlight functional differences between the CLC isoforms and show that isoform mixing influences tissue-specific clathrin function in neurons.

Key Words

Clathrin, neuronal synapse, membrane traffic, coated vesicle formation, protein isoforms

INTRODUCTION

Clathrin mediates membrane traffic and vesicle formation from the plasma membrane and endosomal compartments¹. Recruited by cargo-recognising adaptor proteins, triskelion-shaped clathrin proteins assemble into polyhedral lattices to capture membrane-associated cargo and promote membrane bending into clathrin-coated vesicles (CCVs). Through sequestration of a variety of cargo, CCVs play fundamental roles in general cellular physiology including regulation of nutrient uptake and signalling, as well as in tissue-specific membrane traffic such as synaptic vesicle (SV) generation². This range of clathrin functions has been attributed to adaptor and accessory protein variation³. However, functional diversity is also generated by variability of clathrin subunits. Vertebrates have two types of clathrin heavy chains with distinct functions⁴. The major vertebrate clathrin, responsible for receptor-mediated endocytosis and other housekeeping membrane traffic pathways, is formed from clathrin heavy chain CHC17 (herein referred to as CHC) associated with clathrin light chains (CLCs), which do not bind the minor CHC22 clathrin isoform⁵, which mediates specialised trafficking in muscle cells. Vertebrate CLCs are encoded by two different genes *CLTA* and *CLTB*, producing CLCa and CLCb isoforms of about 60% sequence identity^{6,7}. Their sequence differences have been conserved throughout evolution after their encoding genes arose through duplication, suggesting the two isoforms can mediate distinct functions^{8,9}. Expression levels of the CLCa and CLCb isoforms are tissue-specific¹⁰, and further variation is created by alternative gene splicing during development¹¹ and in brain^{6,7}. Here we address how CLC diversity affects the biophysical properties of clathrin and how the resulting variation affects the specialised function of clathrin in SV recycling.

Clathrin-mediated SV regeneration following degranulation is critical for sustained neurotransmission, and efficient endocytosis is required to maintain synaptic plasma membrane surface area and retrieval of SV proteins¹². However, where exactly clathrin functions in the SV regeneration cycle and whether clathrin is essential to this process is

debated ^{2, 13}. Recent studies suggest that clathrin is mainly involved in SV generation from endosome-like compartments ¹⁴. Dysfunction of the clathrin-associated endocytic machinery results in neurological defects, as observed in a number of diseases such as Parkinson's disease ¹⁵, Alzheimer's disease ³ and in numerous animal models in which clathrin-associated proteins have been genetically deleted, demonstrating the importance of clathrin pathways for neuron function ¹⁶⁻²¹. Notably, like various other endocytic proteins ³, CLCs undergo neuron-specific splicing ²², which introduces one exon in CLCb (encoding 18 residues) and two exons (encoding 30 residues) in CLCa at equivalent positions near the CLC C-termini, resulting in higher molecular weight forms nCLCb and nCLCa ^{6, 7}.

Limited functional differences between CLCa and CLCb have been observed in cell culture with respect to clathrin dynamics ²³, during focal adhesion formation ²⁴ and during cancer cell migration ²⁵, with mechanisms attributed to possible isoform-specific differences in CLC binding proteins and post-translational modification ²⁶. The capacity for biophysical differences in clathrin comprising different CLC isoforms and their splicing variants to influence tissue-specific clathrin functions has not yet been considered. CLC variability has potential to affect clathrin function as a result of CLC interaction with key domains of the clathrin triskelion that contribute to clathrin-mediated membrane bending. CLCs stabilise the triskelion vertex through binding the trimerisation domain (TxD) formed by non-covalent interaction of three CHC subunits ^{27, 28}. From the vertex CLCs extend along the triskelion leg to the characteristic bend at the knee where they regulate conformation ²⁹. CLCs are required for efficient clathrin-mediated membrane vesiculation at low temperature *in vitro* ³⁰ and, in cells, CLCs link CCVs to actin remodelling Hip proteins ^{31, 32} and recruit myosin VIa to clathrin-coated pits (CCPs) ³³. Thus, CLCs affect clathrin-mediated membrane deformation directly through their influence on clathrin lattice properties ^{30, 34} and indirectly through their interaction with the force-generating actin machinery. Loss of CLCs in culture and *in vivo* affects CCV uptake of some, but not all cargo, possibly reflecting variability in mechanical demand for packaging different cargo into CCVs ^{10, 26, 35}.

Here, we assess how clathrin lattices formed with neuronal and non-neuronal CLC variants could differentially affect function by correlating their *in vitro* biophysical properties with *in vivo* neuronal phenotypes of mice lacking CLC-encoding genes. We found that CLC composition significantly influenced clathrin lattice properties and their ability to form vesicles from liposome membranes *in vitro*. CLC splice variation influenced CHC knee conformation and thus assembly curvature, and mixtures of neuronal CLC isoforms produced clathrin lattices that were more effective at membrane deformation than clathrin comprising only one neuronal CLC isoforms. Mice expressing only CLCa or CLCb isoforms showed differences in SV regeneration and synaptic neurotransmission compared to corresponding wild-type (WT) littermates and to each other. Collectively, the functional differences between CLC isoforms presented here establish a role for CLC diversity in regulating neuronal clathrin function in the brain.

RESULTS

CLC splice variants differentially influence lattice curvature via the triskelion knee

The vertex of the clathrin triskelion has a “pucker” at the TxD. Within clathrin lattices, the pucker angle and the crossing angle of interacting CHC legs (Figure 1a) determine the possible overall curvature of spherical assemblies^{36,37}, while the knee bending angle determines whether a hexagon (non-curvature inducing) or pentagon (curvature-inducing) can be formed³⁸. This versatility of clathrin assemblies allow clathrin to sequester cargo of various sizes as well as to form stable, flat assemblies that serve as signalling hubs^{3,39}.

CLCs maintain the puckered conformation of triskelia in flat assemblies³⁰ and structural studies showed that nCLCb can influence conformation of the triskelion knee up to a degree that inhibits assembly²⁹. We therefore hypothesized that sequence differences between the CLC isoforms and their splice variants that occur at the C- and N-termini might modulate CLC influence on triskelion conformation and lattice curvature.

To address this, we produced clathrin triskelia of defined CLC composition by reconstituting tissue-derived CHC triskelia with recombinantly expressed CLCa, CLCb, nCLCa or nCLCb (Supplementary Figure 1a-d)⁴⁰. We then induced assembly of these different clathrins into closed cages⁴¹ and analysed their diameters as a measure of lattice curvature by electron microscopy (Fig. 1b, c). Previous studies showed that tissue-derived, CLC-bound clathrin (native) forms two major size classes, while CHC-only triskelia predominantly form small-sized cages⁴¹⁻⁴⁴. Our results confirmed that without CLCs, assembled CHC formed predominantly cages of less than 90 nm in diameter with an average size of around 70 nm, representing cages of up to 60 triskelia⁴⁴. Clathrin with each of the CLC variants was also able to form larger cages with an average diameter of around 110 nm (140 triskelia) for those cages. The degree to which larger cages were formed varied significantly between splice variants (Fig. 1b, c), indicating that the neuronal splice inserts affect the influence of CLCs on lattice curvature. To establish whether differences in larger cage formation resulted from CLC

influence on the triskelion vertex or on the CHC knee conformation or both, we dissected the effect of CLCs separately for each domain.

To characterise CLC effects at the triskelion vertex, we measured the stability of triskelia with each CLC isoform in the presence of N-lauryl sarcosine detergent (SARC), previously shown to dissociate CHC-CLC trimers into monomers²⁷. Following exposure to increasing amounts of SARC, the proportion of monomers was evaluated by blue-native polyacrylamide gel electrophoresis (BN-PAGE) (Fig. 1d). Calculating the EC₅₀ for triskelion dissociation showed that, compared to CLC-free CHC triskelia, vertex stability was approximately doubled by CLCa variants and approximately tripled by CLCb variants (Figure 1e, f). The neuronal splice inserts had no additional influence on trimer stability, as previously suggested by an isolated study of nCLCb fragments²⁷. The stability of triskelia reconstituted with a 1:1 mixture of CLCa and CLCb (CLCa/b) or nCLCa and nCLCb (nCLCa/b) was similar to that of triskelia with CLCa or nCLCa only (Fig. 1e, f), indicating that dissociation of the least stabilising CLC disrupts the whole triskelion. This latter effect is in agreement with the presence of only trimers and monomers of CHC-CLC complexes and no dimer intermediates (Fig. 1d). While the CLCa and CLCb isoforms stabilised triskelia vertices to different degrees, this did not correlate with the differential effects of CLC variants on cage size, suggesting that CLC influence at the vertex is not a major factor in cage size determination.

We next tested whether CLC diversity affects cage size through an influence on CHC knee conformation. This was assessed by producing clathrin cages from two CHC fragments, the Hub (residues 1074-1675) plus the terminal-distal leg segment (TDD, residues 1-1074, Supplementary Figure 1e), which together constitute a full-length clathrin triskelion “cut” at the knee (Fig. 1g). These CHC fragments can assemble together into full, intact cages⁴⁵ and Hub fragments can be reconstituted with CLCs⁴⁶. Cages produced when TDD was combined with Hub fragments reconstituted with each CLC variant were similar in size to fragment cages without CLCs, and the larger cages observed for CLC variants associated

with intact CHC did not form (Fig. 1c, g, h). This result demonstrates that for CLC diversity to exert an effect on lattice curvature, the CHC knee must be intact and that CLC splice variants differ in their influence on CHC knee conformation. For each closed cage, there is a fixed number of 12 pentagons, but a varying number of hexagons⁴⁷. Thus, larger cages (i.e. lattices of lower curvature) have a smaller pentagon to hexagon ratio. These were predominantly induced to form by neuronal CLCs, suggesting that neuronal splice inserts' influence on the CHC knee reduces the likelihood of pentagon formation and supports hexagon formation.

CLC diversity modulates mechanical properties of the clathrin lattice

We next investigated the mechanical consequences of CLC diversity on clathrin's ability to deform membranes. We previously found that mechanical properties of clathrin lattices were CLC-dependent and that the reduced ability of CLC-free clathrin to bend membranes *in vitro* correlated with poorer planar lattice quality³⁰. To measure lattice quality, clathrins with different CLC composition were assembled on electron microscopy (EM) grids coated with a clathrin-binding fragment of epsin1 (H₆-ΔENTH-epsin¹⁴⁴⁻⁵⁷⁵, Supplementary Figure 1f)⁴⁸. The flat lattices formed were visualized by EM and their periodicity assessed by Fourier transform analysis. We observed that lattice quality was significantly reduced for clathrin with the neuronal splice variants of either CLCa or CLCb compared to clathrin reconstituted with their respective non-neuronal variants (Fig. 2a-c). While lattice quality was not significantly different between clathrin with nCLCa or nCLCb, nCLCb clathrin showed a tendency to form lattices of poorer quality (Fig. 2c) and lattice quality was significantly improved if formed from a mix of nCLCa clathrin and nCLCb clathrin (Fig. 2b and Supplementary Figure 2). Conversely, lattice quality was reduced in mixtures of CLCa clathrin and CLCb clathrin compared to lattices formed by clathrin with only CLCa or CLCb. Notably, the lattice quality resulting from neuronal and non-neuronal CLC compositions correlated with their influence on cage size (Table 1).

To establish how variation in CLC influence affects clathrin's function in membrane bending, we used a low temperature *in vitro* budding assay³⁰. In this system, H₆-ΔENTH-epsin¹⁴⁴⁻⁵⁷⁵, coupled to liposomes via modified Ni-NTA lipids, captures clathrin at the liposome surface. Lattice assembly on these liposomes generates buds, which remain attached to the liposome due to lack of dynamin, needed for scission^{30, 48}. At 37°C, native clathrin and CHC can both efficiently form coated buds, but at 15°C, the liposomes are stiffer and CLC-free clathrin cannot form buds as effectively as native clathrin. We therefore tested the efficiency of clathrin with different CLC composition to form clathrin-coated buds at 15°C. For each clathrin, we measured the diameter of clathrin-coated membrane profiles in thin-section electron micrographs and assessed budding efficiency by the percentage of clathrin-coated buds (defined by a fitted diameter < 200 nm) compared to all clathrin-coated membrane profiles analysed (Fig. 2d). In line with previous findings, we found that at 15°C native clathrin was about twice as efficient in membrane deformation as CLC-free clathrin³⁰, and that budding efficiencies varied with the CLC composition of clathrin tested (Fig. 2e). CLCa or CLCb clathrin lattices vesiculated membrane more efficiently than either neuronal clathrin variant (Fig. 2e and Supplementary Figure 3). We found no statistically significant differences between CLCa and CLCb isoforms of the neuronal or non-neuronal splice variants over the whole data set, yet differences within each experiment indicate that in budding, clathrin with CLCb was slightly more efficient than CLCa clathrin, and nCLCb clathrin potentially less efficient than nCLCa clathrin (Fig. 2f). Notably, mixing reconstituted neuronal clathrins improved their budding efficiency (Fig. 2g). In general, a trend correlating budding efficiency with lattice quality and curvature was observed (Fig. 2g and Table 1). This recurring “mixture effect” suggests that neuronal clathrin benefits from cooperative co-assembly of clathrin with both isoforms.

Membrane deformation could result either from lattice formation at constant curvature or through transitioning from flat to curved lattices (Fig. 2h). To determine how budding was generated in our *in vitro* system and how it was influenced by CLCs, we measured the angle

between the convex side of the coat and the coat-free membrane (Fig. 2h), coat curvature (i.e. diameter of the clathrin-coated structure), coat length and neck width for all coated membrane profiles⁴⁹ and then correlated these measurements. We observed a variety of coat curvatures in our system (Fig. 2i) and found that while neck width decreased with budding angle, as would be expected for both modes of deformation, coat curvature correlated with the budding angle of the coated to the coat-free membrane (Fig 2j, l). This indicates that lattices transition from flat to curved in our system, rather than assembling with constant curvature, which would be independent of budding angle (Fig. 2h). In further support of this, we found no correlation between coat length and budding angle (Fig. 2k). Thus, we conclude that in our *in vitro* system, clathrin initially assembles into flat lattices on the liposome membrane and then gradually deforms the underlying membrane into coated buds, as observed in human SK-MEL-2 cells^{49, 50}. Our results suggest that CLC-mediated regulation is required for the transition of flat to curved lattices and that CLC variants differ in their ability to promote this transition. Thus, collectively from these *in vitro* studies, we conclude that CLC variants differentially regulate triskelion knee conformation within the lattice, affecting the mechanical ability to deform membrane into coated buds. In particular, single neuronal splice variants were less functional in these properties compared to their non-neuronal splice variants, while a mixture of neuronal variants appeared to improve their functionality to non-neuronal levels.

CLC composition affects SV density, motor and brain function

Our *in vitro* experiments indicate that clathrin lattices formed from a mixture of clathrin with each neuronal CLC isoform efficiently support membrane deformation. In comparison, clathrin comprising only one neuronal CLC isoform is attenuated for membrane budding. Therefore, we predicted that neurons in animals with only one CLC isoform might be defective in clathrin-mediated pathways that influence SV formation. This hypothesis was investigated in knock-out (KO) mice lacking the *Cltb* or *Cltc* genes in all tissues (CLCa KO and CLCb KO mice). We produced CLCb KO mice for comparison to our previously

generated CLCa KO mice¹⁰. Loss of *Cltb* in CLCb KO mice was confirmed by PCR, and no CLCb or nCLCb protein was detected in a variety of tissues analysed (Supplementary Figure 4). Whereas wild-type (WT) mice express a mixture of CLCs in most tissues¹⁰, CLCa KO mice express only CLCb or nCLCb, and CLCb KO mice express only CLCa or nCLCa, enabling functional analysis of clathrin with only one type of CLC in neurons. Ongoing breeding of the CLCa KO colony confirmed a 50% survival rate compared to that expected for homozygous CLCa KO mice¹⁰, whereas homozygous CLCb KO mice had no survival defects (Fig. 3a). Given that genetic deletions in clathrin pathways often result in neuronal phenotypes, we assessed performance in the rotarod test for neuro-motor coordination for both CLC KO mice⁵¹. Compared to their WT littermates, surviving CLCa KO mice displayed defects in rotarod balance, whereas CLCb KO mice did not (Fig. 3b). Further assessment of sensorimotor function revealed that CLCa KO mice exhibited defects in a grid-walking test, (Fig. 3c), but not in grip strength (Fig. 3d), suggesting neurological rather than muscular dysfunction in the CLCa KO animals.

Defects in cerebellar neurons could account for impairment in the rotarod performance test⁵². Therefore, we examined the cerebellum of both CLCa KO and CLCb KO mice. H&E staining of the cerebellum revealed no gross abnormalities in either KO strain (Supplementary Figure 5a). As clathrin-mediated pathways can influence SV formation², we next quantified SV number in cerebellar synapses by electron microscopy (Fig. 4a-i). We observed a trend towards reduced numbers of SVs in proximity to the postsynaptic density (PSD) (SV density) of cerebellar synapses in CLCa KO mice compared to their WT littermates (Fig. 4b). In contrast, the CLCb KO mice had similar levels of SVs in cerebellar neurons compared to their WT littermates, correlating with the impairment of rotarod performance observed in the CLCa but not CLCb KO strain (Fig. 4f). Furthermore, there was no change in individual vesicle size (Fig. 4c, g), PSD length (Fig. 4d, h) and overall synapse number (Fig. 4e, i) in both KO strains. These data suggest that defects in SV density in the cerebellum are specific to CLCa KO mice.

To establish whether the apparent SV reduction in CLCa KO mice is characteristic of other brain regions, we also analysed the ultrastructure of excitatory synapses in the CA1 region of the adult hippocampus (Fig. 4j-r and Supplementary Figure 5b), a region of well-defined neuronal architecture and neurophysiological circuitry. Notably, SV density was significantly reduced in hippocampal neurons in the CLCa KO animals and clearly more pronounced than the trend observed in cerebellar synapses. In contrast, SV density in equivalent neurons of the CLCb KO mice was significantly increased compared to their WT littermates (Fig. 4k, o). Interestingly, relative to WT littermates, there was also a trend towards an increase in the overall number of hippocampal excitatory synapses in the CLCb KO mice (Fig. 4r), but no change in synapse density for CLCa KO mice (Fig. 4n). Other parameters such as individual SV size (Fig. 4l, p) and the PSD length (Fig. 4m, q) were similar between both KO strains and respective WT littermates. Thus, CLC composition influences SV density in excitatory neurons of the hippocampus and suggests differential functions for nCLCa and nCLCb in SV generation.

CLCa KO and CLCb KO mice have shared and distinct neurotransmission defects in hippocampal neurons

Acute hippocampal slices are amenable to electrophysiology recordings and hippocampal neurons have frequently been used to study the function of endocytic proteins in synaptic transmission^{14, 16, 17, 19, 20, 53}. We therefore used this system to further evaluate the function of excitatory synapses in the hippocampus of CLCa and CLCb KO animals. To make electrophysiological recordings at Schaffer collateral (SC)-CA1 synapses in acute hippocampal slices, a stimulating electrode was placed in the SC fibres of the CA3 region and responses were then recorded in the CA1 pyramidal cell layer (Fig. 5a). Analyses of the evoked excitatory postsynaptic current (EPSC) responses to stimuli of increasing magnitude revealed decreased EPSC response amplitude in the CLCa KO mice compared to WT littermates, suggesting impaired basal synaptic transmission in the CLCa KO mice (Fig. 5b). In contrast, the evoked EPSC response amplitude in hippocampal slices from the CLCb KO

mice was of similar or higher magnitude than that of their WT littermates, suggesting that basal synaptic transmission was intact and even enhanced (Fig. 5c). These differences in synaptic connectivity between hippocampal function in the two KO strains could arise from defects in presynaptic neurotransmitter release correlating with differences in SV pool size relative to WT littermates (Fig. 4k, o).

To further investigate presynaptic function, we performed paired-pulse ratio (PPR) recordings experiments, an approach that allows assessment of defects in neurotransmitter release⁵⁴.⁵⁵ In excitatory neurons such as those analysed here, a second stimulus pulse (P_2) fired in short succession after an initial pulse (P_1) results in a larger response than the first stimulus. This facilitation is dependent on changes in the probability of neurotransmitter release. PPR is inversely correlated with release probability, as lower initial release probability leaves more fusion-competent vesicles remaining at the terminal which are then released after the second stimulus^{54, 55}. We observed that, compared to WT littermates, the PPR was increased in CLCa KO mice, consistent with a reduction in release probability (Fig. 5d). In contrast, no differences in PPR were observed in CLCb KO mice compared to WT littermates (Fig. 5e). Thus, specific loss of nCLCa impairs presynaptic function compromising neurotransmitter release at the SC-CA1 synapse.

Differences in the number of SVs and the size of the readily releasable pool (RRP), which contains vesicles that are available for release immediately after stimulation⁵⁶, could account for differences in presynaptic function of CLCa and CLCb KO mice (Fig. 5). However, changes in SV fusion efficiency and the rate of SV recycling could also contribute to the phenotype. To investigate these possibilities, we recorded responses to a prolonged high-frequency stimulus, which maximally depletes presynaptic terminals of the RRP. Under these conditions, initial responses would draw from the pre-existing SV pool, while sustained neurotransmission would rely on the efficiency of SV regeneration⁵⁷. Using this approach and first-order correction for vesicle recycling⁵⁷, we were able to assess CLC-dependency

for different stages of SV exo- and endocytosis from these recordings. We found that the initial fusion rate of SVs in either KO strain was similar to that of their WT littermates, indicating that correct packaging of fusion-mediating cargo was not affected by changes in CLC composition (Fig. 6 and Supplementary Figure 6). Instead, both KO models had a decreased SV recycling rate characteristic of defective SV regeneration (Fig. 6). This finding correlated with our expectation from *in vitro* properties of reconstituted clathrin isoforms (Table 1) that showed clathrin lattices with only one type of neuronal CLC were different from mixed lattices in their assembly properties (Fig. 2b) and less efficient in membrane budding than a mix of nCLCa and nCLCb clathrin (Fig. 2g).

Further calculations based on data obtained from sustained trains of action potentials indicated that the RRP was larger in the CLCb KO mice but reduced in the CLCa KO mice when compared to WT littermates (Fig. 6 and Supplementary Figure 6). This is in agreement with the respective reduction and enhancement of SV density observed in the ultrastructural analyses of their hippocampal neurons (Fig. 4j-r). Together, these data show that CLCs are required for efficient and sustained synaptic function. These results further suggest that loss of either CLC decreases the ability of acute SV regeneration, but that the KO strains differ in their ability to generally maintain SV pools. Neurons with only nCLCa clathrin apparently compensate for defective SV recycling by expanding their SV pool, while neurons with only nCLCb clathrin cannot compensate and show impaired SV recycling plus decimated SV pools.

To get a better understanding of the potential pathways involved in SV pool differences between CLCa and CLCb KO mice, we analysed protein expression levels of synaptic markers, SV cargo and players in the endocytic pathway in the hippocampus (Fig. 7a, Supplementary Figure 7). We found no significant differences in the protein levels of various major SV proteins involved in SV fusion, such as synaptobrevin, for either CLCa or CLCb KO mice, indicating no defects in cargo packaging in the hippocampus (Fig. 7b), as suggested

from our electrophysiology data. As CHC levels were differentially affected in the KO strains with partial reduction in the hippocampus of CLCa but not CLCb KO mice (Fig. 7b), we attribute the recycling defect characteristic of both KO strains (Fig. 6) to loss of CLC diversity rather than decrease of CHC levels. Further supporting the idea that the phenotypes observed arise directly from CLC loss is the observation that SV pools were not as affected in cerebellar synapses, although CHC levels were reduced to similar levels in both tissues for each genotype (Fig. 7 and Supplementary Figure 8).

Comparing normalized hippocampal levels of accessory proteins and proteins involved in SV function between the two KO strains (Fig. 7b) made it possible to identify pathways specifically associated with loss of one CLC isoform. Levels of neuronal adaptor protein AP180 were significantly reduced in CLCa but not CLCb KO mice compared to WT strains, which could result from the reduction of CHC in the CLCa KO animals and thus impairment of CCV formation involved in regenerating SVs¹⁶. Notably, the hippocampus from CLCb KO mice (with enlarged SV pools) had significantly elevated levels of the endocytic membrane-bending proteins epsin1⁵⁸ and amphiphysin1⁵⁹, as well as decreased levels of the uncoating accessory protein auxilin and the endocytic adaptor AP2 relative to the CLCa KO strain. These changes are consistent with compensatory membrane traffic mechanisms leading to increased SV numbers in the CLCb KO mice through increased endosomal traffic and altered clathrin dynamics at the plasma membrane.

Levels of the vesicular GABA transporter Vgat, associated with loading inhibitory SVs, were reduced in both KO strains, yet more pronounced in the CLCa KO mice, whereas the levels of the vesicular glutamate transporter Vglut1 associated with loading excitatory SVs were unchanged (Fig. 7), suggesting that inhibitory synapses are more severely affected by the loss of either CLC than the excitatory synapses. The often tonic activity in inhibitory synapses⁶⁰ likely exacerbates the effects of CLC loss, and increased susceptibility to endocytic defects in inhibitory synapses, as has been reported for the loss of other endocytic

components^{16, 17, 61-63}. Levels of the postsynaptic glutamate receptor GluR1 were significantly reduced only in the CLCb KO mice, reflecting possible compensation⁶⁴ for producing an excess of excitatory SVs (Fig. 4o) and enhanced basal neurotransmission (Fig. 5c). Finally, the level of N-cadherin, a synaptic cell adhesion protein, was significantly increased in the hippocampus of the CLCb KO strain compared to the CLCa KO strain, corresponding to the trend for increased synapse density and activity observed in these animals (Fig. 4r)⁶⁵.

Overall, the neurotransmission defects in animals with only CLCa or CLCb isoforms were consistent with the biophysical data that neuronal CLC splicing creates clathrin with properties that rely on a mixture of both neuronal CLCs for efficient budding to replenish SV pools (Fig. 2, Table 1). In addition, the phenotypes of the KO animals indicate that neuronal CLC isoforms are differentially able to support compensatory mechanisms for adjusting SV pools in hippocampal synapses, suggesting that clathrin with nCLCa is more functional than clathrin with nCLCb, which corresponds to the biophysical properties of lattices formed by these clathrins (Fig. 2c, f).

DISCUSSION

To understand the consequences of CLC diversity for clathrin function, we characterised the biophysical properties of *in vitro* assemblies formed from clathrin comprising single CLC isoforms and correlated these properties with neuronal phenotypes observed in KO animals expressing single CLC isoforms. We found that neuronal CLC splicing affects lattice properties (Fig. 1b and Fig. 2b) by diversifying the CLC's influence on the CHC knee to regulate lattice curvature (Fig. 1c, g) and deform membrane (Fig. 2e). CLC splicing apparently influences clathrin's ability to introduce pentagons in order to transition from flat to curved lattices (Fig. 1 and Fig. 2). Our *in vitro* studies further showed that lattices formed from mixtures of clathrin with nCLCa and nCLCb have different assembly properties and are more efficient in membrane budding compared to clathrin with only one type of neuronal CLC (Fig. 2b, g). Consistent with this observation, neurons from both CLCa and CLCb KO mice showed electrophysiological defects in synaptic transmission that indicated clathrin-dependent SV recycling was impaired (Fig. 5 and Fig. 6). While the CLCa KO mice had reduced numbers of SVs in their hippocampal synapses, the CLCb KO mice had more SVs than their WT littermates (Fig. 4k, o). Thus, although SV recycling was impaired in both KO strains, clathrin with only nCLCa (in the CLCb KO mice) was able to support a compensatory pathway of SV formation, but clathrin with only nCLCb (in the CLCa KO) was not (Fig. 6, 7). These findings establish functional differences between CLC isoforms *in vivo* and also demonstrate how CLC diversity is important for clathrin function in neurons.

There are several pathways involved in SV recycling in neurons and the role of clathrin has been widely debated, possibly because the contribution of each pathway to SV formation is variable between organisms, types of neurons and stimulus^{53, 66, 67}. After SVs are exocytosed, their membrane and contents must be recaptured from the plasma membrane to maintain SV pools and the plasma membrane surface area¹². This can either be achieved by direct re-generation of SVs through CME from the plasma membrane at low-frequency

stimulus, or through clathrin-independent mechanisms such as activity-dependent bulk endocytosis and endophilin-dependent ultra-fast endocytosis, which predominantly mediate retrieval of SV components from the plasma membrane under high stimulus^{2, 13, 14, 19, 53}. However, in most systems at high-frequency stimulus, it is the rapid clathrin-dependent trafficking of SV proteins from the endosomal pathway that leads to re-sorting and formation of SVs², which can occur in a timeframe of 1-3 seconds after stimulation¹⁴. In our analysis of neurotransmission, SV recycling defects were detected by electrophysiology within three seconds at high stimulus (20 Hz for 3s), suggesting the defects detected were due to impaired clathrin-mediated generation of SVs from endosomes (Fig. 8a). These findings are consistent with previously observed roles for CLCs in recycling from non-neuronal endosomal compartments^{68, 69}.

Neuronal splicing predominates for CLCb in neurons⁷⁰, while neuronal CLCs are not present in other brain cells such as glial or Schwann cells²², indicating that the CLC splice variants segregate within brain cell types. That an SV recycling defect (in response to sustained high frequency stimulus) was shared by neurons in both CLC KO strains fits with our *in vitro* biophysical data that demonstrate single neuronal CLCs are not as efficient in membrane deformation as a mixture of clathrin with both neuronal CLCs (Fig. 2g). However, we found that clathrin with only nCLCa generated an increased steady-state SV pool in CLCb KO neurons, possibly in reaction to this defect, while clathrin with only nCLCb could not. Increased levels of epsin1 and amphiphysin1 in the CLCb KO hippocampus suggests that these endocytic accessory proteins might be involved in enabling a compensatory pathway. Both proteins comprise membrane curvature-inducing domains (ENTH and BAR domains, respectively) to facilitate endocytosis^{58, 59}. Thus, they are likely to improve the efficiency of nCLCa-only clathrin lattices in coated-vesicle formation (Fig. 8a). CLCa seems to have preferential connection with the actin cytoskeleton compared to CLCb^{24, 33}, which might further account for the ability of nCLCa clathrin to function on its own without nCLCb and benefit from involvement of accessory molecules. In the (normal) presence of nCLCb, the

actin interactions of nCLCa may be “diluted down”, so that the presence of nCLCb works as an attenuating balancing mechanism to control SV pools and neurotransmission by more efficient lattice formation, as opposed to using accessory factors. Considering the whole animal phenotypes, including the increased mortality rate for CLCa but not CLCb KO animals, CLCa seems to be the more functional CLC, while CLCb functions mainly in conjunction with CLCa. This is in line with the observation that CLC expression ratios vary with tissue, and while lymphoid cells almost exclusively express CLCa, no tissue has been found to express exclusively CLCb^{10, 71}. In addition, CLC isoform ratios transiently change during cell differentiation, development, tumour progression^{11, 25, 70} and cell migration⁶⁸.

The *in vitro* data presented here confirm that CLCs stabilise the TxD and provide functional evidence for their regulation CHC knee conformation (Fig. 1)^{29, 72}. This CLC-mediated regulation of triskelion conformation promoted the formation of larger cages (Fig. 1) and prevents excessive distortion of triskelia within assemblies^{30, 73}. CLCs further enhanced the efficiency to deform membrane through lattice rearrangement (Fig. 2), a process more feasible in the presence of weak intermolecular bonds between triskelia⁷⁴. Thus, we conclude that through controlling CHC’s conformational flexibility, CLCs reduce excessive interactions between triskelia and promote lattice rearrangement. Weakening interactions between triskelia further explains how CLCs raise the critical assembly concentration for clathrin^{41, 75} and create dynamic lattices amenable to regulation by adaptor proteins^{34, 76}. Moreover, neuronal CLC splicing had a significant influence on lattice curvature and budding efficiency, decreasing the likelihood of forming pentagons over hexagons (Table 1), which was attributable to effects on the CHC knee domain (Fig. 1g). Given that the inserted sequences are located near the TxD where the C-termini of CLCs are bound (arrowheads, Fig. 8b), we propose that the splice inserts affect the conformation of the adjacent knee of a neighbouring triskelion, which is closer than the knee of the triskelion to which the CLC is bound (Fig. 8c). This intermolecular influence could involve splice inserts at the C-terminus (stars, Fig. 8c) interacting with the neighbouring CHC or with the N-terminal domain of a CLC

bound to the neighbouring knee (Ns, Fig. 8c). Considering the average 40% sequence differences between CLCa and CLCb isoforms and their even greater variation at the N-terminus, inter-CLC interactions could vary depending on which splice isoform interacts with which CLC isoform N-terminus, thereby influencing overall lattice properties. This imputed interaction may be lost from clathrin with non-neuronal CLCs, which would explain why mixing non-neuronal CLC isoforms does not affect *in vitro* budding to the same extent as mixing neuronal CLC isoforms (Fig. 2g).

Here we characterise the properties of homo- and hetero-assemblies of clathrin comprising single CLC isoforms. In brain, CLC isoforms are apparently randomly distributed on triskelia⁷⁷. Nevertheless, in the latter scenario, the neuronal inserted sequences would still influence lattice curvature via interactions with an adjacent triskelion knee and the presence of (n)CLCb would serve as an attenuator of (n)CLCa-specific interactions as we have proposed. Further, in cells where CLCb expression is transiently increased⁶⁸, newly synthesized triskelia would be generally occupied by a single CLC isoform as clathrin subunit turnover is slow⁷¹. The resulting homotypic clathrins would then participate mixed in lattices, as we have studied here. Thus (n)CLCb expression levels (and/or local abundance within cells) could tailor clathrin lattice properties specifically to particular cellular needs.

In summary, this study reveals functional differences between CLCa and CLCb splicing variants *in vitro* and between neuronal CLC isoforms *in vivo*, indicating that the two neuronal CLCs work together for optimal clathrin function in neurons. Our findings demonstrate the importance of CLC diversity for synaptic transmission and illustrate how CLC variability expands the complexity of clathrin to serve tissue-specific functions.

METHODS

Protein expression and purification

His-tagged epsin1 in pET32c and His-tagged Δ ENTH-epsin¹⁴⁴⁻⁵⁷⁵ in pQE32 were expressed and purified as previously described by standard nickel affinity chromatography and size exclusion chromatography on a Superdex 200 10/300 GL column (GE Healthcare)⁷⁸. CLCs in pET28a were expressed with a thrombin-cleavable, N-terminal His-tag and purified by standard nickel affinity chromatography and further polished by size exclusion chromatography on a Superdex 200 10/300 GL column (GE Healthcare). His-tags of CLC constructs were removed by thrombin cleavage.

CCVs were purified from porcine brain as described previously⁴¹ and clathrin triskelia purified by tris-extraction and size exclusion chromatography on a Superose 6 Increase 10/300 GL column (GE Healthcare). To generate CHC-only triskelia, endogenous CLCs were removed using NaSCN and separated from CHC by size exclusion chromatography⁴⁰.

For reconstitution of clathrin of defined CLC composition, CHC in buffer C (50 mM Tris-HCl pH 8.0, 50 mM NaCl, 2mM EDTA, 1mM DTT) at 0.8-1.0 mg/ml was incubated with purified CLCs at 0.7 – 1.0 mg/ml in in the same buffer or in 20 mM Tris-HCl pH 8.0, 200 mM NaCl at a 1:6.6 ratio (w/w) for 1 h on ice.

Electron microscopy

Freshly glow-discharged, homemade, carbon-coated formvar films on copper grids (Agar Scientific) were used for all EM applications. All specimens were observed using a Tecnai G2 (FEI) electron microscope at an acceleration voltage of 120 kV. Images were obtained using a SIS Morada digital camera and TIA software (FEI).

Cage size and lattice curvature determination

Samples were dialysed in assembly-promoting buffer A. Assembled cages were adsorbed to EM grids by placing grids on 10 µl droplets of samples at 0.2 mg/ml on Parafilm for 90 s. Excessive liquid was removed using filter paper before grids were washed twice by transferring grids sequentially onto two 15 µl droplets of buffer A containing 2 mM CaCl₂. Samples were then stained with 2% uranyl acetate in water for 1 min and air-dried before subjected to EM analysis. Diameters of clathrin cages were measured from electron micrographs using ImageJ software (NIH). Distribution of diameters was averaged from the size distribution of 200 cages from three independent sets of experiments. For quantification of the proportion of the two cage populations, grouped into cages smaller or larger than 90nm in diameter, the proportions of the area under the curve for each population and experiment were averaged and tested for statistically significant differences between reconstituted clathrin isoforms using Prism 6 (GraphPad).

Trimer Stability

Reconstituted clathrin isoforms at a concentration of 1 mg/ml were dialysed overnight in 10 mM Tris pH 8.0 at 4°C. 2 µg of clathrin isoforms were diluted in 10 mM Tris pH 8.0 containing 0%, 0.01%, 0.02%, 0.05%, 0.1%, 0.2% or 0.5% N-Lauroylsarcosine (SARC) to a final volume of 20 µl. After 5-10 min incubation on ice, SDS-free 4× loading dye (250 mM Tris pH 6.8, 40% glycerine, 0.02% bromophenol blue) was added to the samples and samples loaded onto an SDS-free 6 % acrylamide gel to resolve mixtures of clathrin trimers and monomers using a BN-PAGE set-up. Two different running buffers, anode buffer (24.8 mM Tris-base, 192 mM glycine) and cathode buffer (24.8 mM Tris-base, 192 mM Glycine, 0.02% Coomassie Blue G250) were used for gel electrophoresis. All buffers were pre-chilled to 4°C and the chamber set-up placed on ice during electrophoresis. Electrophoresis was carried out at 40 V for 15 min, then for 40 min at 90 V. Subsequently, the cathode buffer was exchanged for another cathode buffer of lower Coomassie concentration (24.8 mM Tris-base, 192 mM glycine, 0.002% Coomassie Blue G250) and electrophoresis continued for 2 h

at 4°C. Samples were then transferred to nitrocellulose membrane and analysed by western blotting using TD.1 antibody for CHC and X16 or CLTB antibody for CLCs (see list of antibodies below). Intensities of ECL-developed western blot signals were used to measure the relative amounts of clathrin populations within one sample using ImageJ software (NIH). Data from 3-5 repeats per reconstituted clathrin isoform were pooled and plotted against the logarithmic transform of detergent concentration and fitted using Prism 6 software (GraphPad).

Lattice assembly and quality assessment

For incubation, EM grids were placed on 5-15 µl droplets on Parafilm at room temperature. Grids were firstly incubated with 0.04 mg/ml tag-free epsin 1 or H₆-ΔENTH-epsin¹⁴⁴⁻⁵⁷⁵ in buffer G (25 mM HEPES pH 7.2, 125 mM potassium acetate, 5 mM magnesium acetate) for 30 min. Unbound protein was removed by transferring grids to two droplets of buffer G before incubating grids with clathrin at 0.05 mg/ml in buffer G containing 0.1% BSA for 30 min. Lattices were fixed with 3% glutaraldehyde in buffer G for 15 min and stained with 2% or 5% uranyl acetate in water for 1 min. Lattice regularity was assessed from electron micrographs of similar quality and various focuses for each specimen as a measure of lattice quality³⁰. For this, 2D Fast Fourier Transform (FFT) was produced using ImageJ software (NIH). The height of the peak corresponding to the periodicity of the lattice (at ~0.036 nm⁻¹) served as a measure for lattice quality – the higher the peak, the higher the quality of the lattice. 5-12 images were analysed for each reconstituted clathrin isoform within each of three independent sets of experiments.

In vitro budding assay

In vitro budding was performed as previously described⁴⁸. In brief, H₆-ΔENTH-epsin¹⁴⁴⁻⁵⁷⁵ were bound to liposomes made from brain polar lipid extracts containing 5% DGS-Ni-NTA lipids (Avanti). H₆-ΔENTH-epsin¹⁴⁴⁻⁵⁷⁵-coated liposomes were then chilled to 15°C and mixed

with clathrin triskelia stock solutions at 15°C, incubated for 30 min at 15°C and then transferred on ice. Samples were then fixed at 4°C overnight and processed for EM analysis. Diameter, coat length, budding angle and neck width of clathrin-coated membrane profiles were measured from electron micrographs using ImageJ (NIH) and data processed using Prism (GraphPad). Between 150 and 200 coat profiles, randomly sampled across four thin sections, were analysed for each sample (> 60 000 nm total coat length per experiment per sample). The proportion of curved lattices, defined by a diameter of less than 200 nm, of all lattice profiles examined, was used as a measure of budding efficiency. Results from 3-5 independent sets of experiments were tested for statistical significance.

Generation of CLC KO mice

The *Cltb*^{ko/ko} mouse strain used for this research project was created from ES cell clone 19159A-F4, generated by Regeneron Pharmaceuticals, Inc., and obtained from the KOMP Repository (www.komp.org). Methods used to create the CLCb-null ES cell clone have previously been published ⁷⁹. In brief, the complete coding region of the *Cltb* gene was completely deleted by homologous recombination using a large BAC-based targeting vector. Targeted ES cells were then injected into albino C57BL/6J-N blastocytes and transferred into foster mothers. Chimeric offspring were mated with C57BL/6J females (Charles River), and germ-line transmission of the *Cltb*-null allele (*Cltb*^{ko}) was established. Heterozygote *Cltb*^{ko/+} mice were backcrossed on the C57BL/6 background and bred to produce *Cltb*^{ko/ko} homozygous mice. CLCa KO mice were derived from C57BL/6 WT mice ¹⁰.

Mouse behavioural tests

All experiments were performed in accordance with the Animals Scientific procedures Act UK (1986). Heterozygous *Cltb*^{ko/+} mice were crossed to obtain homozygous *Cltb*^{ko/ko} mice and WT littermates. Heterozygous *Clta*^{ko/+} mice were crossed to obtain homozygous *Clta*^{ko/ko} mice and WT littermates. Experiments were performed in 2-3-month-old mice. Both male and

female mice were used for the rotarod experiment. Male mice only were used for all other behavioural experiments.

Rotarod latency (Accelerating Rotarod; Ugo-Basile 7650 model) was used to assess motor coordination. Mice were placed on the Rotarod, which was slowly accelerated from 3 to 30 rounds per minute over 5 minutes. Mice were given 3 trials per day for 2 days with at least 10 min inter-trial intervals. Time to fall from the rotarod (latency) was recorded for each trial. Mice that remained on the Rotarod for the whole 5 min trial were assigned a 300 second latency.

Grip strength (grip strength meter; Columbus Instruments) was used to measure muscle strength in the forepaws. The grip strength meter was positioned horizontally, and mice were held by the tail and allowed to grasp the metal pull-bar. The animals were then pulled back and the force applied to the bar and the moment the grasp was released was recorded. Mice were given 5 trials with 1 min inter-trial intervals and were tested on 2 days. The mean of results from 10 trials was assigned for the grip strength of each animal.

Grid-walking was used to assess spontaneous motor deficits and limb movements involved in precise stepping, coordination, and accurate paw placement. Adult mice were required to navigate over a wire mesh grid. After each trial, 70% ethanol was used to clean the apparatus. Mice were given 3 trials with 1 min inter-trial intervals and were tested on 2 days. Behaviour on the grid was recorded on camera and was analysed later by an experimenter who was blind to the genotype. A foot-slip was scored when the paw completely missed a rung and the limb fell between the rungs. Counts of foot-slips for right forelimb, left forelimb, right hindlimb and left hindlimb were obtained. Total footsteps were also recorded. The mean of results from 10 trials was used for each animal.

Electron microscopy of synapse ultrastructure

Experiments were performed in 4-12-month-old mice. Female mice were used for ultrastructural experiments. Brain hemispheres were collected from homozygous KO mice and WT littermates and cut in sagittal orientation. Slices were fixed in 2% paraformaldehyde and 1.5% glutaraldehyde and stained sequentially with 1.5% potassium ferricyanide and 1% OsO₄, 1% thiocarbohydrazide, 2% OsO₄, 1% uranyl acetate, 0.66% lead nitrate in aspartic acid. Samples were then gradually dehydrated and embedded for electron microscopy. The ultrastructure of excitatory synapses in four electron micrographs of the VI lobule of the cerebellum or CA1 hippocampus perinuclear region per genotype were analysed for the ultrastructure of excitatory synapses using ImageJ (NIH) and Prism 6 (GraphPad) software (n = 3). To determine SV density, SVs in 300 nm vicinity to the centre of the PSD in each synapse were counted.

Quantification of protein expression in brain

Mouse hippocampus and cerebellum were harvested from six 9-12-month old C57BL/6 WT and homozygous CLCa and CLCb KO mice and quickly snap-frozen in liquid nitrogen and stored at -80°C until further use. Tissue were quickly thawed and homogenised in lysis buffer (50 mM HEPES pH 8.0, 50 mM NaCl, 1% Triton-X 100, 5 mM EDTA, 2 mM CaCl₂, 1 mM PMSF, cOmplete™ Protease Inhibitor Cocktail mix (Roche)). The homogenate was further incubated on ice for 45 min before centrifugation at 21 000 g and 4°C for 2 x 10 min in an Eppendorf 5424 R benchtop centrifuge (Eppendorf). Protein content of the lysate was determined by BCA assay (Thermo Fisher). For analysis, 25 µg of sample were loaded on 4-15% acrylamide gels (Bio-Rad) and subjected to SDS-PAGE and western blotting.

List of antibodies

Antigen	Antibody name/clone	Species	Source	Catalogue No	WB dilution	WB solution
beta-Actin	clone AC-15	mouse	Sigma-Aldrich	A5441	1:3000	5% milk PBS-T
Amphiphysin 1	EP2060Y	rabbit	Abcam	ab52646	1:25000	5% milk TBS-T
AP-1	88/Adaptin γ	mouse	BD Transduction	610386	1:500	5% milk PBS-T
AP-2	AP6	rabbit	self-made		1:1000	5% milk PBS-T
AP180		rabbit	Synaptic Systems	155003	1:1000	5% milk TBS-T
Auxilin	Anti-DNAJC6	rabbit	Abcam	ab103321	1:100	2% BSA TBS-T
CHC	TD.1	mouse	self-made		1:2000	5% milk PBS-T
CLCa	X16	mouse	self-made		1:1000	5% milk PBS-T
CLCb	CLTB	rabbit	Proteintech	10455-1-AP	1:1000	5% milk PBS-T
Dynamin I	Dynamin-I (3G4B6)	mouse	Cell Signaling Technology	4565S	1:2000	5% milk TBS-T
Endophilin 1	E1E6Q	rabbit	Cell Signaling Technology	65169	1:1000	5% BSA TBS-T
Epsin 1	Anti-Epsin 1 ERP3023	rabbit	Abcam	ab75879	1:500	5% milk TBS-T
GluR1	D4N9V	rabbit	Cell Signaling Technology	13185	1:1000	5% milk TBS-T
HIP1R		rabbit	Millipore	AB9882	1:500	2% BSA TBS-T
Hsc70	3A3	mouse	Thermo Fisher	MA3006	1:1000	5% milk TBS-T
LRRK2	MJFF2 (c41-2)	rabbit	Abcam	ab133474	1:1000	2% BSA TBS-T
N-Cadherin	32/N-Cadherin	mouse	BD Transduction	610920	1:1000	5% milk PBS-T
PiCALM	Anti-PiCALM	rabbit	Sigma-Aldrich	HPA019061	1:500	5% milk PBS-T
SNAP25	clone 71.1	mouse	Synaptic Systems	111-011	1:1500	5% milk TBS-T
Synaptobrevin 2	Clone 69.1	mouse	Synaptic Systems	104211	1:2000	5% milk TBS-T
Synaptophysin 1		rabbit	Synaptic Systems	101-002	1:5000	5% milk TBS-T
Synaptotagmin 1/2		rabbit	Synaptic Systems	105-002	1:1000	5% milk TBS-T
Syntaxin	78.2	mouse	Synaptic Systems	110-001	1:1000	5% milk TBS-T
VGAT		guinea pig	Synaptic Systems	131004	1:1000	5% milk TBS-T
VGLUT1		guinea pig	Millipore	ab5905	1:5000	5% BSA TBS-T

Electrophysiology

Experiments were performed in 8-10-month-old mice. Both male and female mice were used for electrophysiological experiments. Acute transverse hippocampal slices (300 μ m) of homozygous CLCa or CLCb KO and control mice were cut on a Leica VT-1000 vibratome in ice-cold artificial cerebrospinal fluid (ACSF) bubbled with 95% O₂/5% CO₂ containing (in mM): NaCl (125), KCl (2.4), NaHCO₃ (26), NaH₂PO₄ (1.4), D-(+)-Glucose (20), CaCl₂ (0.5) and MgCl₂ (3). At 5-minute intervals, slices were then transferred into a series of 3 different chambers oxygenated (95% O₂/5% CO₂) in the same base ACSF but with the following temperature and component (in mM) variations: **1.** 21°C initially with MgCl₂ (1) and CaCl₂ (0.5) then allowed to heat gradually to 36°C; **2.** 36°C with MgCl₂ (1) and CaCl₂ (1); and **3.** 36°C initially with MgCl₂ (1) and CaCl₂ (2) before cooling to 21°C. Slices were then left for at least 1 hr before recordings commenced.

Evoked recordings were performed on an upright microscope continually perfused with oxygenated recording solution at room temperature containing the same ACSF composition as the third chamber and supplemented with 10 μ M bicuculline. Pyramidal cells in the CA1 region were held at -60mV in whole-cell voltage-clamp configuration using glass microelectrodes (resistance 3-8 M Ω) filled with caesium gluconate intracellular solution containing (in mM): D-gluconic acid lactone (130), HEPES (10), EGTA (10), NaCl (10), CaCl₂ (0.5), MgCl₂(1), ATP (1) and GTP (0.5), QX314 (5), pH to 7.2 with CsOH. To evoke postsynaptic EPSCs, a bipolar concentric stimulation electrode (FHC) was placed in the SC fibres of the CA3 region. For input-output recordings, the stimulus pulse was varied between 0.2 and 1mA with a pulse width of 0.1 ms and stimuli were delivered at a rate of 0.1 Hz. Paired pulse stimuli were given at rate of 0.2 Hz with different inter-stimulus intervals, ranging from 50 ms to 200 ms and a stimulation strength set to approximately 50% of the maximal response for each cell. PPR was calculated as the ratio of the peak amplitude of the second response over the first response. Calculation of RRP size, initial fusion efficiency and SV recycling rate was done on ESPC recordings that underwent 3 s duration trains of

stimulation at 20Hz and estimated as previously described^{57, 80}. Briefly, RRP, fusion efficiency (fe) and vesicle recycling rate (α) were evaluated from the cumulative charge during the stimulation train using the following two equations:

$$\text{Equation 1: } fe = \frac{r(1)}{r(\infty)} (1 - \exp(-\alpha\Delta t))$$

$$\text{Equation 2: } fe = \frac{r(1)}{\sum_{i=1}^s r(i) \exp(-\alpha(S-i)\Delta t)}$$
$$fe = \frac{r(1)}{\sum_{i=1}^s r(i) \exp(-\alpha(S-i)\Delta t)}$$

$r(1)$ is the charge of the first EPSC in the train

$r(i)$ the charge passed by the i th EPSC

$r(\infty)$ was calculated from the average charge of the last 10 EPSCs in the train

Δt is the stimulus interval in the train

The RRP was estimated as $RRP=r(1)/fe$.

All currents were recorded using an Axopatch 200B amplifier, filtered (1 kHz) and digitised (10 kHz). Data were monitored online and analysed offline using WinEDR and WinWCP software (available free online at http://spider.science.strath.ac.uk/sipbs/software_ses.htm). Stimulus artefacts in representative traces were digitally removed for clarity.

Statistical analysis

All experiments were performed at least three times. All calculations and graphs were performed with ImageJ, Microsoft Excel and GraphPad Prism software. P-values were calculated using two-tailed Student's unpaired or paired (*in vitro* budding) t-tests, two-way ANOVA with repeated measures (electrophysiology), one-way ANOVA followed by Holm-Sidak correction for multiple comparison or one-way ANOVA for preselected pairs without correction for multiple comparison (clathrin biophysical properties). Detailed statistical

information including statistical tests used, number of independent experiments, *p* values and definition of error bars is listed in individual figure legends.

ACKNOWLEDGMENTS

This work was supported by grants to F. M. B. from the Wellcome Trust (107858/Z/15/Z) and to P.C.S. from the Medical Research Council (MR/M024083/1). L. R. was supported by a Wellcome Trust 4-year interdisciplinary PhD studentship. J. J. B. was supported by MRC funding to the MRC Laboratory of Molecular Cell Biology at UCL, award code MC_U12266B. P. N. D. was supported by a UCL Excellence Fellowship. The authors would like to thank UCL IQPath, UCL Institute of Neurology, Queen Square London, WC1N 3BG for processing tissue slices for H&E staining and Massimo Signore (ICH) and Anna Crowley (KLB Transgenic facility, UCL) for the generation of the *Cltb*^{ko} mouse strain.

AUTHOR CONTRIBUTIONS

The study was conceived by L. R. and F. M. B. with expert input from P. N. D., F. M., E. P. V. and P. C. S. Electrophysiology experiments were conducted and analysed by F. M. All *in vitro* reconstitution, protein level and EM experiments and analyses were carried out by L. R. with expert assistance from J. J. B., F. M., E. P. V., P. N. D. and K. B. Mouse behaviour data and survival characteristics were collected by M. D. C. and Y. C. The paper was written by L. R., F. M. B., F. M. and P. C. S. and then all authors read and commented on the paper.

COMPETING INTEREST

The authors declare no competing interest.

FIGURE LEGENDS

Fig. 1: CLCs differentially regulate lattice curvature and vertex stability. **a** Pucker (1) and knee (2) angles of the clathrin triskelion (black: CHC, blue: CLC) dictate lattice architecture. Different knee angles (encircled, black straight and dashed lines) are adopted for hexagon (non-curvature inducing) or pentagon (curvature inducing) formation (3), whole triskelion in black and parts of others in grey. Lattice curvature is further amended through changes in pucker angle (dashed and black lines) (4), or changes in proximal leg-crossing angle (5). CLC subunits are omitted for simplicity. **b** Diameter distributions of *in vitro* assemblies formed from clathrin reconstituted with indicated CLCs, 1:1 mixtures of reconstituted clathrins (CLCa/b or nCLCa/b) or CHC only (CHC), determined from electron micrographs (mean, $n = 3$, > 200 cages per experiment). The smaller class of cages (< 90 nm in diameter) is highlighted in the frequency distributions as shaded areas under the curves and quantified (bottom right) as a percentage of cages formed (mean \pm SEM, $*P < 0.05$, $***P < 0.001$ one-way ANOVA followed by Holm-Sidak correction for multiple comparison, $n = 3$). **c** Overlay of cage size distributions shown in **b**. **d** Representative immunoblots for CLCb-reconstituted clathrin (CLCb) and CHC-only (CHC), which were incubated with increasing concentration (w/v) of N-lauryl sarcosine (SARC) detergent. Trimers and monomers were separated by native gel and proportions determined by immunoblotting using TD.1 antibody. The presence of CLCb bound to CHC (bottom panel, lane 1-7) was assessed by immunoblotting CLTB antibody and compared to free CLCb (lane 8). **e** Dissociation profiles established as in **d** for clathrin reconstituted with indicated CLC isoforms, clathrin reconstituted with a 1:1 mix of CLCs or CHC alone ($3 < n < 7$) were fitted using an EC_{50} shift model. **f** EC_{50} ratio for dissociation from **d** (mean \pm SEM, $*P < 0.05$, $**P < 0.01$, one-way ANOVA, $3 < n < 7$). **g** Size distributions of cages formed from TDD (black) and Hub (grey) co-assemblies, with Hub fragments reconstituted or not with the different CLC isoforms or 1:1 mixtures thereof. **h**

Representative EM images of cages formed from full-length CHC (top) or Hub/TDD fragments (bottom) without or following reconstitution with CLC isoforms. Scale bar: 100 nm.

Fig. 2: CLC splicing affects *in vitro* lattice properties. **a** Clathrin reconstituted with indicated CLC isoforms and mixtures thereof were assembled into flat lattices and visualised by negative stain for EM analysis. Scale bar: 200 nm. **b** Quality (regularity quantified by Fourier transform) of lattices generated as in **a**, (mean \pm SEM, * $P < 0.05$, ** $P < 0.01$, one-way ANOVA followed by Holm-Sidak correction for multiple comparison, $n = 5$). **c** Differences in lattice quality between indicated reconstituted clathrins in individual experiments in **b** (data points and mean \pm SEM, $n = 5$). **d** Representative EM images of clathrin reconstituted with indicated CLC isoforms, 1:1 mixtures thereof, CHC only (CHC) and tissue-derived clathrin (native) assemblies on H₆- Δ ENTH-epsin¹⁴⁴⁻⁵⁷⁵-coated liposomes. Scale bar: 200 nm. **e** Quantification of the percentage of curved lattices (defined as coats with < 200 nm fitted diameter) of $> 60\,000$ nm total coat profiles generated as in **d** (mean \pm SEM, * $P < 0.05$, ** $P < 0.01$, paired Student's t-test for native and CHC, $n = 3$, one-way ANOVA with repeated measures for CLC-reconstituted clathrin, $n = 4$). **f** Differences in percentage of curved lattices between indicated reconstituted clathrins in individual experiments in **e** (data points and mean \pm SEM, $n = 4$). **g** Quantification of budding efficiency (% curved lattices determined as in **e**, normalised to native) of reconstituted clathrins and mixtures thereof (* $P < 0.05$, one-way ANOVA for sets of neuronal or non-neuronal samples, $n = 3$). **h** Parameters characterising coated buds (top); coat length c , membrane bud diameter d , neck width n , and budding angle θ . Models of clathrin-mediated membrane deformation by transitional curvature generation and lattice rearrangement (middle) or lattice growth under constant lattice curvature (bottom). **i** Representative coat profiles for flat (left), curved (middle) and budded (right) structures. **j** to **l** Analysis of the dataset generated as shown in **d** for bud parameters d (**j**), c (**k**) and n (**l**) as shown in **h** in relation to the θ of each structure measured for all reconstituted clathrins within the same experiment. Inserts in **j** and **k** show the different correlations of these parameters

as predicted according to the curvature transition (red, straight line) constant curvature models (red, dashed line) shown in **h**.

Fig. 3: CLCa and CLCb KO mice display different survival and behavioural phenotypes. **a** Genotype distribution for CLCa KO (n = 590) and CLCb KO (n = 359) mice after weaning compared to expected distribution (**** $P < 0.0001$, *Chi-square* test). **b** Performance in the accelerated rotarod test (latency to fall) by CLC KO (CLCa KO = 12, CLCb KO = 9) and control wild-type littermates (CLCa WT = 12, CLCb WT = 10) expressed as data points and mean \pm SEM (** $P < 0.01$, unpaired Student's t-test). **c** Time to cross grid for CLCa KO (n = 10) and control mice (n = 10) expressed as data points and mean \pm SEM (* $P < 0.05$, unpaired Student's t-test). **d** Grip strength of CLCa KO (n = 10) and control mice (n = 11, gram-force relative grip strength over body weight) expressed as data points and mean \pm SEM.

Fig. 4: SV pool size is differentially affected in CLCa and CLCb KO mice. **a** Representative EM images of excitatory synapses in the molecular layer of cerebellar lobule VI of CLCa WT, CLCa KO, CLCb WT and CLCb KO mice. Scale bars: 300 nm. **b** to **i** Quantification of data extracted from EM images as in **a**. Graphs show SV density (pool size) within 300 nm of the postsynaptic density (PSD) (**b** and **f**), frequency distribution of SV size (**c** and **g**), PSD length (**d** and **h**) and synapse density (synapse number per 10 μm^2 area) (**e** and **i**) expressed as mean \pm SEM (* $P < 0.05$, unpaired Student's t-test, n = 4). **j** Representative EM images of excitatory synapses in the CA1 region of the hippocampus of CLCa WT, CLCa KO, CLCb WT and CLCb KO. Scale bars; 300 nm. **k** to **r** Quantification of data extracted from EM images as in **j**. Graphs show SV density within 300 nm of the PSD (**k** and **o**), cumulative frequency distribution of SV size (**l** and **p**), PSD length (**m** and **q**) and synapse density (**n** and **r**) expressed as mean \pm SEM (* $P < 0.05$, unpaired Student's t-test, n = 3).

Fig. 5: CLC composition regulates synaptic function of hippocampal neurons. **a** Schematic illustration of stimulating and recording electrode setup in hippocampal slices. The synapses investigated are formed by a Schaffer-collateral (SC) axon (black) from a pyramidal neuron (black triangles, cell bodies) in the CA3 region synapsing with a receiving pyramidal neuron (grey triangle, cell body) in the CA1 region from which responses are recorded. Black circles denote dentate gyrus (DG) granule cell bodies. **b** Input-output relationship of evoked excitatory postsynaptic currents (EPSCs) at CA1 synapses of WT and CLCa KO hippocampus slices. Traces show responses of representative cells at increasing stimulus intensity with an average of 3 responses for each stimulus strength (mean \pm SEM; $n = 9-11$ slices from 3 animals/genotype; $*P < 0.05$, two-way ANOVA with repeated measures). **c** Input-output relationship of evoked EPSCs at CA1 synapses of WT and CLCb KO hippocampus slices. Traces show response of representative cells at increasing stimulus intensity with an average of 3 responses for each stimulus strength (mean \pm SEM; $n = 12-15$ slices from 3 animals/genotype; $*P < 0.05$, two-way ANOVA with repeated measures). **d** Paired-pulse ratio (PPR) of evoked EPSCs at CA1 synapses of WT and CLCa KO hippocampal slices. Traces show responses of representative cells. Graph displays the mean PPR ($P_2/P_1 \pm$ SEM) from all cells ($n = 9-11$ slices from 3 animals/genotype) at different time intervals between paired pulses ($***P < 0.001$, unpaired Student's t-test). **e** PPR of EPSCs at CA1 synapses of WT and CLCb KO hippocampal slices. Traces show responses of representative cells. Graph displays the mean PPR ($P_2/P_1 \pm$ SEM) from all cells ($n = 12-15$ slices from 4 animals/genotype) at different time intervals between paired pulses.

Fig. 6: SV recycling is impaired in both CLC KO strains and only the CLCb KO strain can compensate. **A** Representative traces of EPSCs following a 20 Hz electrical stimulation for 3 s in CLCa KO and WT hippocampal slices (left). Graphs (right) show the mean (\pm SEM) initial fusion efficiency, recycling rate and readily releasable pool (RRP) size calculated for all cells ($n = 9-11$ slices from 3 animals/genotype; $*P < 0.05$ and $**P < 0.01$, unpaired Student's t-

test). **g** Representative traces of EPSCs following a 20 Hz electrical stimulation for 3 s in CLCb KO and WT hippocampus slices (left). Graphs (right) show the mean (\pm SEM) initial fusion efficiency, recycling rate and RRP size calculated for all cells ($n = 11-12$ slices from 4 animals/genotype; $*P < 0.05$, unpaired Student's t-test)

Fig. 7: Protein levels change differentially upon loss of CLCa or CLCb in mouse

hippocampus. **a** Representative immunoblots for levels of proteins involved in CCV and SV membrane traffic, neurotransmission and synapse architecture in hippocampal tissue from WT and CLCa KO and CLCb KO mice. The migration position of molecular mass markers is indicated in kilodaltons (kDa) at the left of immunoblots. **b** Quantification of protein levels in hippocampal tissue from CLCa and CLCb KO mice relative to WT mice (mean \pm SEM, $n = 6$ per genotype). Changes in protein expression for each KO strain were assessed for significant differences compared to their WT littermates ($*P < 0.05$, unpaired Student's t-test, see Supplementary Figure 7) and analysed here to establish if these differences were also significant compared to each other ($*P < 0.05$, unpaired Student's t-test). Black stars indicate statistically significant differences compared to WT, but not the other KO. Red stars indicate statistically significant differences compared to WT and the other KO.

Fig. 8: Model of how neuronal CLC diversity regulates synaptic vesicle recycling and lattice properties. **a** In WT mice (centre), a mix of nCLCa and nCLCb clathrin creates the appropriate biophysical properties to mediate SV generation from endosomal compartments (and possibly the plasma membrane). Loss of nCLCa (left) creates nCLCb clathrin lattices, which are defective in efficient SV regeneration, resulting in decimated SV pools. Loss of nCLCb (right) creates nCLCa clathrin lattices, which are also less efficient in SV regeneration than WT (red X), but able to recruit excess accessory proteins to compensate for this defect (red arrow), leading to an overall increased SV pool. **b** CLC (cyan) neuronal splice inserts (arrowheads) are located near the TxD of the bound CHC (green, left, PDB: 3LVH). **c** CLC

(cyan) neuronal splice inserts (stars) are near the CHC knee of the neighbouring triskelion (red or orange) within lattices (right, PDB: 3IYV). Interaction between a neuronal splicing insert and the knee of an adjacent triskelion and/or adjacent CLC N-terminus (N) could promote conformational change in the CHC knee. As the formation of pentagons and hexagons requires different knee angles this interaction could consequently influence lattice curvature (see Fig. 1a).

REFERENCES

1. Brodsky, F.M. Diversity of clathrin function: new tricks for an old protein. *Annu Rev Cell Dev Biol* **28**, 309-336 (2012).
2. Soykan, T., Maritzen, T. & Haucke, V. Modes and mechanisms of synaptic vesicle recycling. *Curr Opin Neurobiol* **39**, 17-23 (2016).
3. McMahon, H.T. & Boucrot, E. Molecular mechanism and physiological functions of clathrin-mediated endocytosis. *Nat Rev Mol Cell Biol* **12**, 517-533 (2011).
4. Dannhauser, P.N. *et al.* CHC22 and CHC17 clathrins have distinct biochemical properties and display differential regulation and function. *J Biol Chem* **292**, 20834-20844 (2017).
5. Liu, S.H. *et al.* A novel clathrin homolog that co-distributes with cytoskeletal components functions in the trans-Golgi network. *EMBO J* **20**, 272-284 (2001).
6. Kirchhausen, T. *et al.* Clathrin heavy chain: molecular cloning and complete primary structure. *Proc Natl Acad Sci U S A* **84**, 8805-8809 (1987).
7. Jackson, A.P., Seow, H.F., Holmes, N., Drickamer, K. & Parham, P. Clathrin light chains contain brain-specific insertion sequences and a region of homology with intermediate filaments. *Nature* **326**, 154-159 (1987).
8. Wakeham, D.E. *et al.* Clathrin heavy and light chain isoforms originated by independent mechanisms of gene duplication during chordate evolution. *Proc Natl Acad Sci U S A* **102**, 7209-7214 (2005).
9. Fumagalli, M. *et al.* Genetic diversity of CHC22 clathrin impacts its function in glucose metabolism. *eLife* **8** (2019).
10. Wu, S. *et al.* Clathrin light chains' role in selective endocytosis influences antibody isotype switching. *Proc Natl Acad Sci U S A* **113**, 9816-9821 (2016).
11. Giudice, J. *et al.* Alternative splicing regulates vesicular trafficking genes in cardiomyocytes during postnatal heart development. *Nat Commun* **5**, 3603 (2014).
12. Heuser, J.E. & Reese, T.S. Evidence for recycling of synaptic vesicle membrane during transmitter release at the frog neuromuscular junction. *J Cell Biol* **57**, 315-344 (1973).
13. Watanabe, S. & Boucrot, E. Fast and ultrafast endocytosis. *Curr Opin Cell Biol* **47**, 64-71 (2017).
14. Watanabe, S. *et al.* Clathrin regenerates synaptic vesicles from endosomes. *Nature* **515**, 228-233 (2014).
15. Soukup, S.F., Vanhauwaert, R. & Verstreken, P. Parkinson's disease: convergence on synaptic homeostasis. *EMBO J* **37**, e98960 (2018).
16. Koo, S.J. *et al.* Vesicular Synaptobrevin/VAMP2 Levels Guarded by AP180 Control Efficient Neurotransmission. *Neuron* **88**, 330-344 (2015).

17. Cao, M. *et al.* Parkinson Sac Domain Mutation in Synaptojanin 1 Impairs Clathrin Uncoating at Synapses and Triggers Dystrophic Changes in Dopaminergic Axons. *Neuron* **93**, 882-896.e885 (2017).
18. Milosevic, I. *et al.* Recruitment of Endophilin to Clathrin-Coated Pit Necks Is Required for Efficient Vesicle Uncoating after Fission. *Neuron* **72**, 587-601 (2011).
19. Kononenko, Natalia L. *et al.* Clathrin/AP-2 Mediate Synaptic Vesicle Reformation from Endosome-like Vacuoles but Are Not Essential for Membrane Retrieval at Central Synapses. *Neuron* **82**, 981-988 (2014).
20. Yim, Y.-I. *et al.* Endocytosis and clathrin-uncoating defects at synapses of auxilin knockout mice. *Proc Natl Acad Sci USA* **107**, 4412 (2010).
21. Mitsunari, T. *et al.* Clathrin adaptor AP-2 is essential for early embryonal development. *Mol Cell Biol* **25**, 9318-9323 (2005).
22. Wong, D.H. *et al.* Neuron-specific expression of high-molecular-weight clathrin light chain. *J Neurosci* **10**, 3025-3031 (1990).
23. Mettlen, M. *et al.* Endocytic Accessory Proteins Are Functionally Distinguished by Their Differential Effects on the Maturation of Clathrin-coated Pits. *Mol Biol Cell* **20**, 3251-3260 (2009).
24. Tsygankova, O.M. & Keen, J.H. A unique role for clathrin light chain a in cell spreading and migration. *J Cell Sci* (2019).
25. Chen, P.H. *et al.* Crosstalk between CLCb/Dyn1-Mediated Adaptive Clathrin-Mediated Endocytosis and Epidermal Growth Factor Receptor Signaling Increases Metastasis. *Dev Cell* **40**, 278-288.e275 (2017).
26. Maib, H., Ferreira, F., Vassilopoulos, S. & Smythe, E. Cargo regulates clathrin-coated pit invagination via clathrin light chain phosphorylation. *J Cell Biol* **217**, 4253 (2018).
27. Ybe, J.A. *et al.* Light Chain C-Terminal Region Reinforces the Stability of Clathrin Heavy Chain Trimers. *Traffic* **8**, 1101-1110 (2007).
28. Chu, D.S., Pishvaei, B. & Payne, G.S. The Light Chain Subunit Is Required for Clathrin Function in *Saccharomyces cerevisiae*. *J Biol Chem* **271**, 33123-33130 (1996).
29. Wilbur, J.D. *et al.* Conformation switching of clathrin light chain regulates clathrin lattice assembly. *Dev Cell* **18**, 841-848 (2010).
30. Dannhauser, P.N. *et al.* Effect of clathrin light chains on the stiffness of clathrin lattices and membrane budding. *Traffic* **16**, 519-533 (2015).
31. Chen, C.Y. & Brodsky, F.M. Huntingtin-interacting protein 1 (Hip1) and Hip1-related protein (Hip1R) bind the conserved sequence of clathrin light chains and thereby influence clathrin assembly in vitro and actin distribution in vivo. *J Biol Chem* **280**, 6109-6117 (2005).
32. Wilbur, J.D. *et al.* Actin binding by Hip1 (huntingtin-interacting protein 1) and Hip1R (Hip1-related protein) is regulated by clathrin light chain. *J Biol Chem* **283**, 32870-32879 (2008).


33. Biancospino, M. *et al.* Clathrin light chain A drives selective myosin VI recruitment to clathrin-coated pits under membrane tension. *Nature Communications* (2019) doi:10.1038/s41467-019-12855-6.
34. Lherbette, M., Redlingshofer, L., Brodsky, F.M., Schaap, I.A.T. & Dannhauser, P.N. The AP2 adaptor enhances clathrin coat stiffness. *FEBS J* **286**, 4074-4085 (2019).
35. Stachowiak, J.C., Brodsky, F.M. & Miller, E.A. A cost-benefit analysis of the physical mechanisms of membrane curvature. *Nat Cell Biol* **15**, 1019-1027 (2013).
36. den Otter, W.K., Renes, M.R. & Briels, W.J. Self-assembly of three-legged patchy particles into polyhedral cages. *J Phys: Condens Matter* **22**, 104103 (2010).
37. Fotin, A. *et al.* Molecular model for a complete clathrin lattice from electron cryomicroscopy. *Nature* **432**, 573-579 (2004).
38. Musacchio, A. *et al.* Functional organization of clathrin in coats: combining electron cryomicroscopy and X-ray crystallography. *Mol Cell* **3**, 761-770 (1999).
39. Baschieri, F. *et al.* Frustrated endocytosis controls contractility-independent mechanotransduction at clathrin-coated structures. *Nat Commun* **9**, 3825 (2018).
40. Winkler, F.K. & Stanley, K.K. Clathrin heavy chain, light chain interactions. *EMBO J* **2**, 1393-1400 (1983).
41. Ungewickell, E. & Ungewickell, H. Bovine brain clathrin light chains impede heavy chain assembly in vitro. *J Biol Chem* **266**, 12710-12714 (1991).
42. Nandi, P.K., Pretorius, H.T., Lippoldt, R.E., Johnson, M.L. & Edelhoch, H. Molecular properties of the reassembled coat protein of coated vesicles. *Biochemistry* **19**, 5917-5921 (1980).
43. Van Jaarsveld, P.P., Nandi, P.K., Lippoldt, R.E., Saroff, H. & Edelhoch, H. Polymerization of clathrin protomers into basket structures. *Biochemistry* **20**, 4129-4135 (1981).
44. Heuser, J. & Kirchhausen, T. Deep-etch views of clathrin assemblies. *J Ultrastruct Res* **92**, 1-27 (1985).
45. Greene, B., Liu, S.H., Wilde, A. & Brodsky, F.M. Complete reconstitution of clathrin basket formation with recombinant protein fragments: adaptor control of clathrin self-assembly. *Traffic* **1**, 69-75 (2000).
46. Liu, S.-H., Wong, M.L., Craik, C.S. & Brodsky, F.M. Regulation of Clathrin Assembly and Trimerization Defined Using Recombinant Triskelion Hubs. *Cell* **83**, 257-267 (1995).
47. Schein, S. Architecture of clathrin fullerene cages reflects a geometric constraint--the head-to-tail exclusion rule--and a preference for asymmetry. *J Mol Biol* **387**, 363-375 (2009).
48. Dannhauser, P.N. & Ungewickell, E.J. Reconstitution of clathrin-coated bud and vesicle formation with minimal components. *Nat Cell Biol* **14**, 634-639 (2012).

49. Avinoam, O., Schorb, M., Beese, C.J., Briggs, J.A.G. & Kaksonen, M. Endocytic sites mature by continuous bending and remodeling of the clathrin coat. *Science* **348**, 1369-1372 (2015).
50. Scott, B.L. *et al.* Membrane bending occurs at all stages of clathrin-coat assembly and defines endocytic dynamics. *Nat Commun* **9**, 419 (2018).
51. Shiotsuki, H. *et al.* A rotarod test for evaluation of motor skill learning. *J Neurosci Methods* **189**, 180-185 (2010).
52. Lalonde, R., Bensoula, A.N. & Filali, M. Rotorod sensorimotor learning in cerebellar mutant mice. *Neuroscience Research* **22**, 423-426 (1995).
53. Watanabe, S. *et al.* Ultrafast endocytosis at mouse hippocampal synapses. *Nature* **504**, 242-247 (2013).
54. Dobrunz, L.E. & Stevens, C.F. Heterogeneity of release probability, facilitation, and depletion at central synapses. *Neuron* **18**, 995-1008 (1997).
55. Zucker, R.S. & Regehr, W.G. Short-term synaptic plasticity. *Annu Rev Physiol* **64**, 355-405 (2002).
56. Kaeser, P.S. & Regehr, W.G. The readily releasable pool of synaptic vesicles. *Curr Opin Neurobiol* **43**, 63-70 (2017).
57. Wesseling, J.F. & Lo, D.C. Limit on the role of activity in controlling the release-ready supply of synaptic vesicles. *J Neurosci* **22**, 9708-9720 (2002).
58. Ford, M.G.J. *et al.* Curvature of clathrin-coated pits driven by epsin. *Nature* **419**, 361-366 (2002).
59. Slepnev, V.I., Ochoa, G.-C., Butler, M.H. & De Camilli, P. Tandem Arrangement of the Clathrin and AP-2 Binding Domains in Amphiphysin 1 and Disruption of Clathrin Coat Function by Amphiphysin Fragments Comprising These Sites. *J Biol Chem* **275**, 17583-17589 (2000).
60. Häusser, M. & Clark, B.A. Tonic Synaptic Inhibition Modulates Neuronal Output Pattern and Spatiotemporal Synaptic Integration. *Neuron* **19**, 665-678 (1997).
61. Ferguson, S.M. *et al.* A selective activity-dependent requirement for dynamin 1 in synaptic vesicle endocytosis. *Science* **316**, 570-574 (2007).
62. Koch, D. *et al.* Proper synaptic vesicle formation and neuronal network activity critically rely on syndapin I. *EMBO J* **30**, 4955-4969 (2011).
63. Hayashi, M. *et al.* Cell- and stimulus-dependent heterogeneity of synaptic vesicle endocytic recycling mechanisms revealed by studies of dynamin 1-null neurons. *Proc Natl Acad Sci USA* **105**, 2175 (2008).
64. Song, I. & Huganir, R.L. Regulation of AMPA receptors during synaptic plasticity. *Trends Neurosci* **25**, 578-588 (2002).
65. Mendez, P., De Roo, M., Poglia, L., Klausner, P. & Muller, D. N-cadherin mediates plasticity-induced long-term spine stabilization. *J Cell Biol* **189**, 589 (2010).

66. Heerssen, H., Fetter, R.D. & Davis, G.W. Clathrin Dependence of Synaptic-Vesicle Formation at the *Drosophila* Neuromuscular Junction. *Curr Biol* **18**, 401-409 (2008).
67. Sato, K. *et al.* Differential requirements for clathrin in receptor-mediated endocytosis and maintenance of synaptic vesicle pools. *Proc Natl Acad Sci U S A* **106**, 1139-1144 (2009).
68. Majeed, S.R. *et al.* Clathrin light chains are required for the gyrating-clathrin recycling pathway and thereby promote cell migration. *Nat Commun* **5**, 3891 (2014).
69. Poupon, V. *et al.* Clathrin light chains function in mannose phosphate receptor trafficking via regulation of actin assembly. *Proc Natl Acad Sci USA* **105**, 168-173 (2008).
70. Stamm, S. *et al.* Clathrin light chain B: gene structure and neuron-specific splicing. *Nucleic Acids Res* **20**, 5097-5103 (1992).
71. Acton, S.L., Brodsky, F. M. Predominance of clathrin light chain LCb correlates with the presence of a regulated secretory pathway. *J Cell Biol* **111**, 1419-1426 (1990).
72. Ybe, J.A., Mishra, S., Helms, S. & Nix, J. Crystal structure at 2.8 Å of the DLLRKN-containing coiled-coil domain of huntingtin-interacting protein 1 (HIP1) reveals a surface suitable for clathrin light chain binding. *J Mol Biol* **367**, 8-15 (2007).
73. Ferguson, M.L. *et al.* Conformation of a clathrin triskelion in solution. *Biochemistry* **45**, 5916-5922 (2006).
74. Saleem, M. *et al.* A balance between membrane elasticity and polymerization energy sets the shape of spherical clathrin coats. *Nat Commun* **6**, 6249 (2015).
75. den Otter, W.K. & Briels, W.J. The Generation of Curved Clathrin Coats from Flat Plaques. *Traffic* **12**, 1407-1416 (2011).
76. Bucher, D. *et al.* Clathrin-adaptor ratio and membrane tension regulate the flat-to-curved transition of the clathrin coat during endocytosis. *Nat Commun* **9**, 1109 (2018).
77. Kirchhausen, T., Harrison, S.C., Parham, P. & Brodsky, F.M. Location and distribution of the light chains in clathrin trimers. *Proc Natl Acad Sci U S A* **80**, 2481-2485 (1983).
78. Kalthoff, C., Alves, J., Urbanke, C., Knorr, R. & Ungewickell, E.J. Unusual Structural Organization of the Endocytic Proteins AP180 and Epsin 1. *J Biol Chem* **277**, 8209-8216 (2002).
79. Valenzuela, D.M. *et al.* High-throughput engineering of the mouse genome coupled with high-resolution expression analysis. *Nat Biotechnol* **21**, 652-659 (2003).
80. Ciani, L. *et al.* Wnt signalling tunes neurotransmitter release by directly targeting Synaptotagmin-1. *Nat Commun* **6**, 8302 (2015).

TABLES

Table 1: Regulation of clathrin lattice properties by CLC isoforms

	high						low
Lattice curvature (pentagon:hexagon ratio)	CLCb	CLCa	nCLCa/b	CLCa/b	nCLCa	nCLCb	
Lattice quality	CLCb	CLCa	nCLCa/b	CLCa/b	nCLCa	nCLCb	
Budding efficiency	CLCb	CLCa	nCLCa/b	CLCa/b	nCLCa	nCLCb	

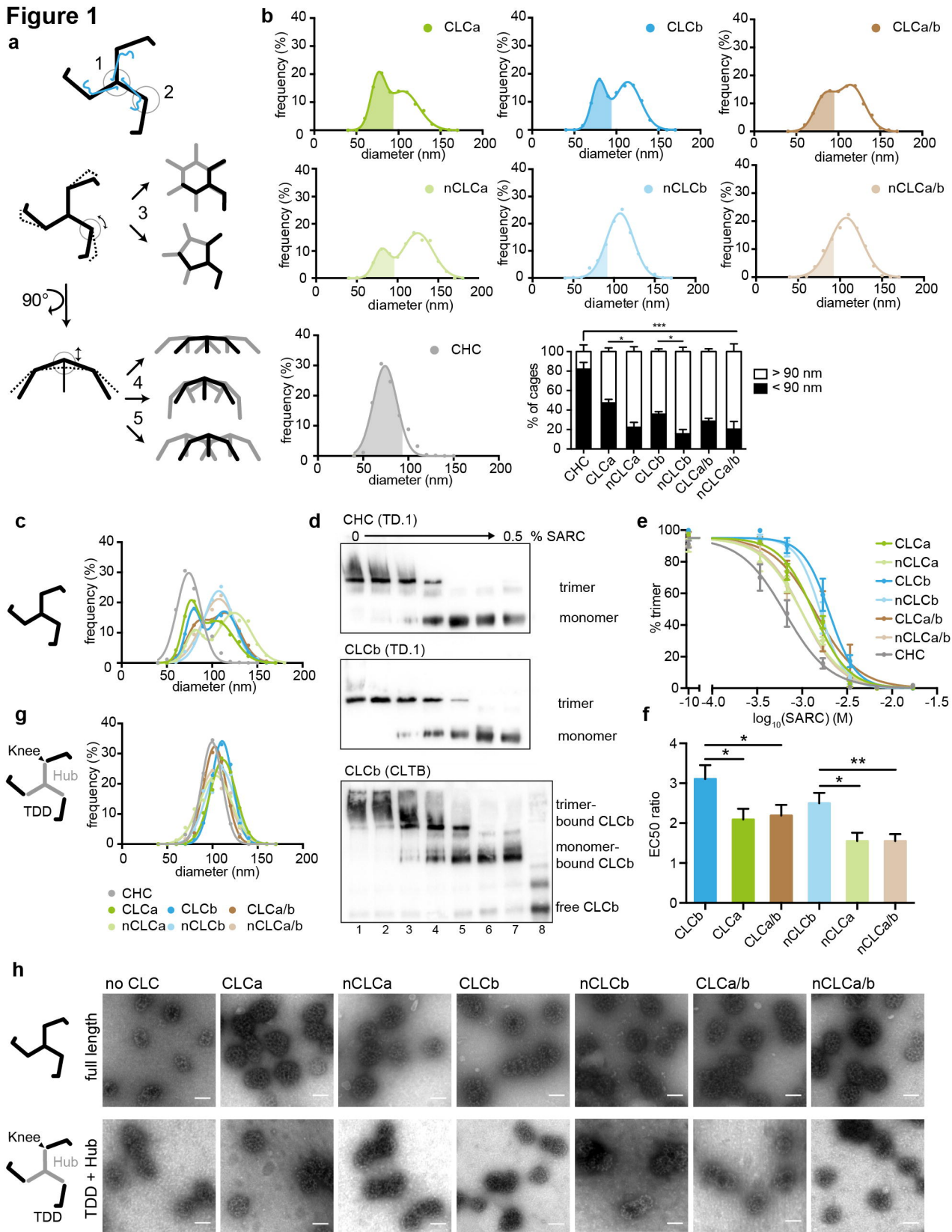


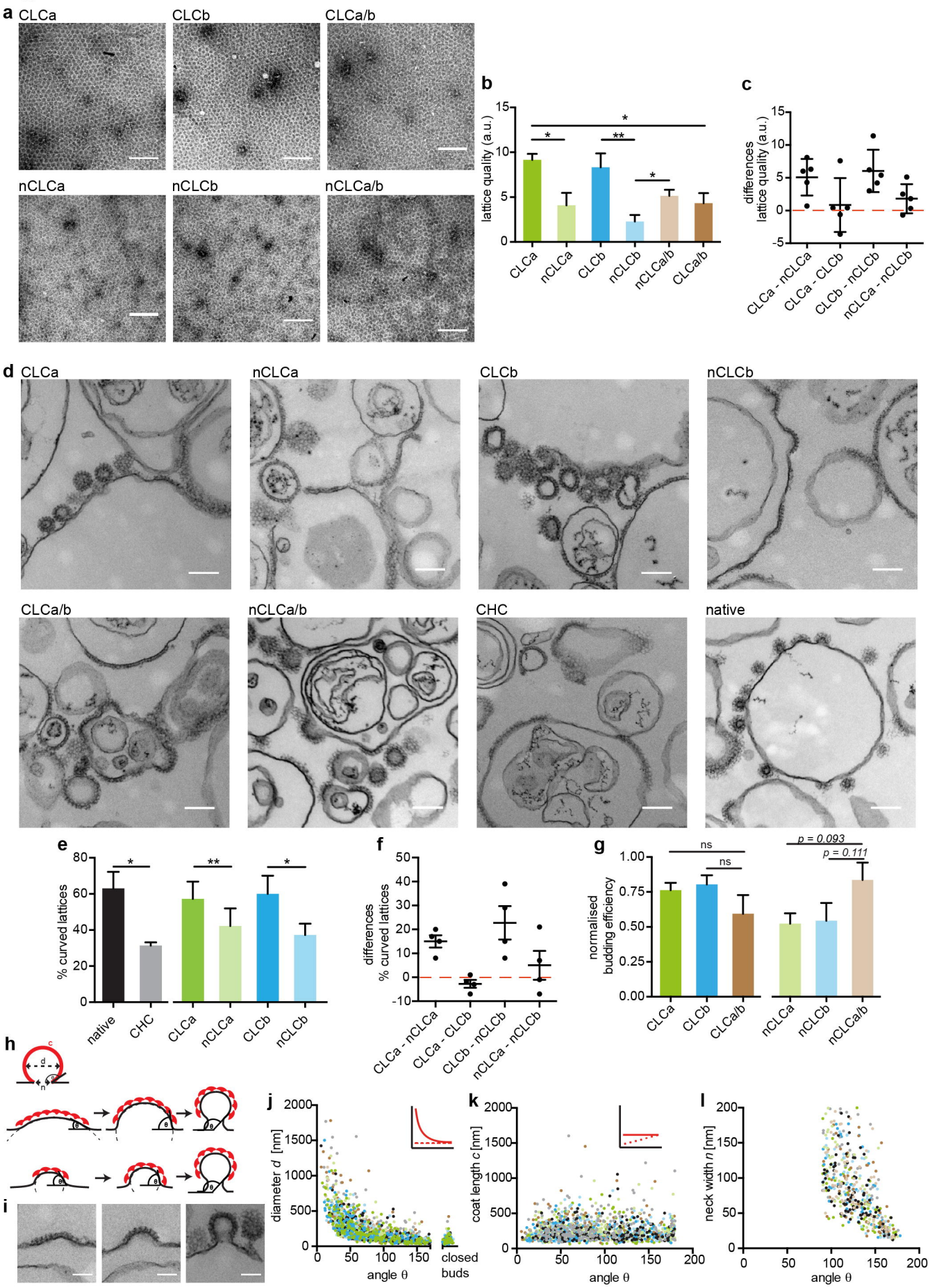
Figure 2

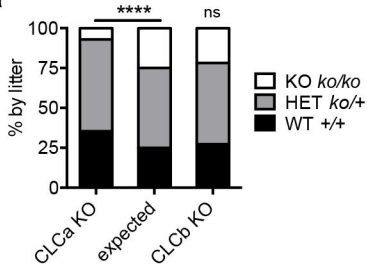
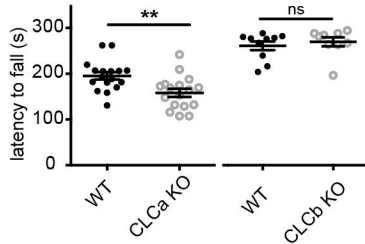
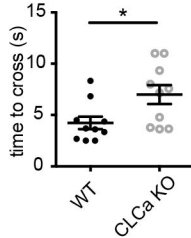
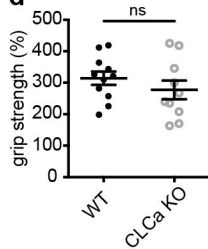
Figure 3**a****b****c****d**

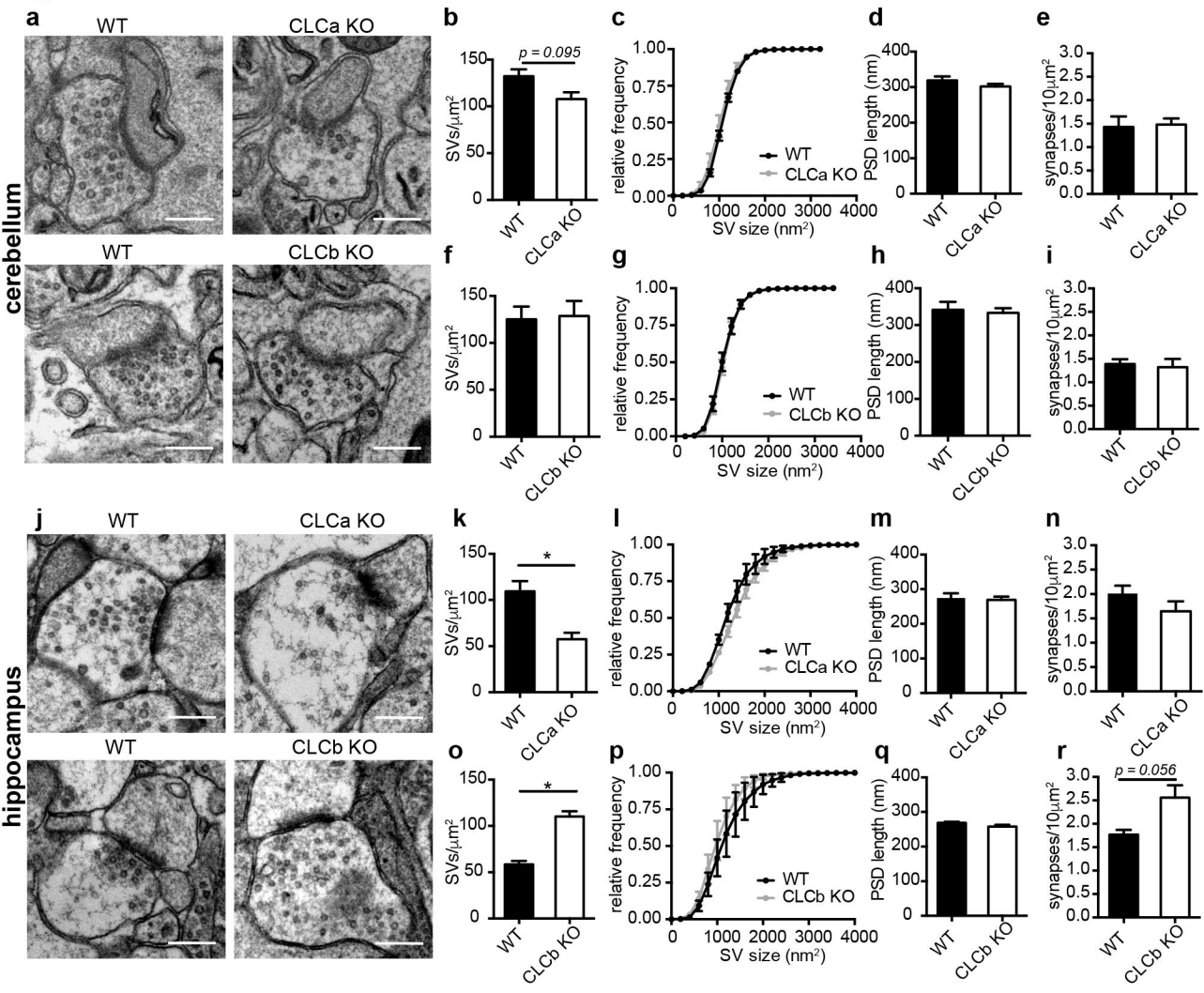
Figure 4

Figure 5

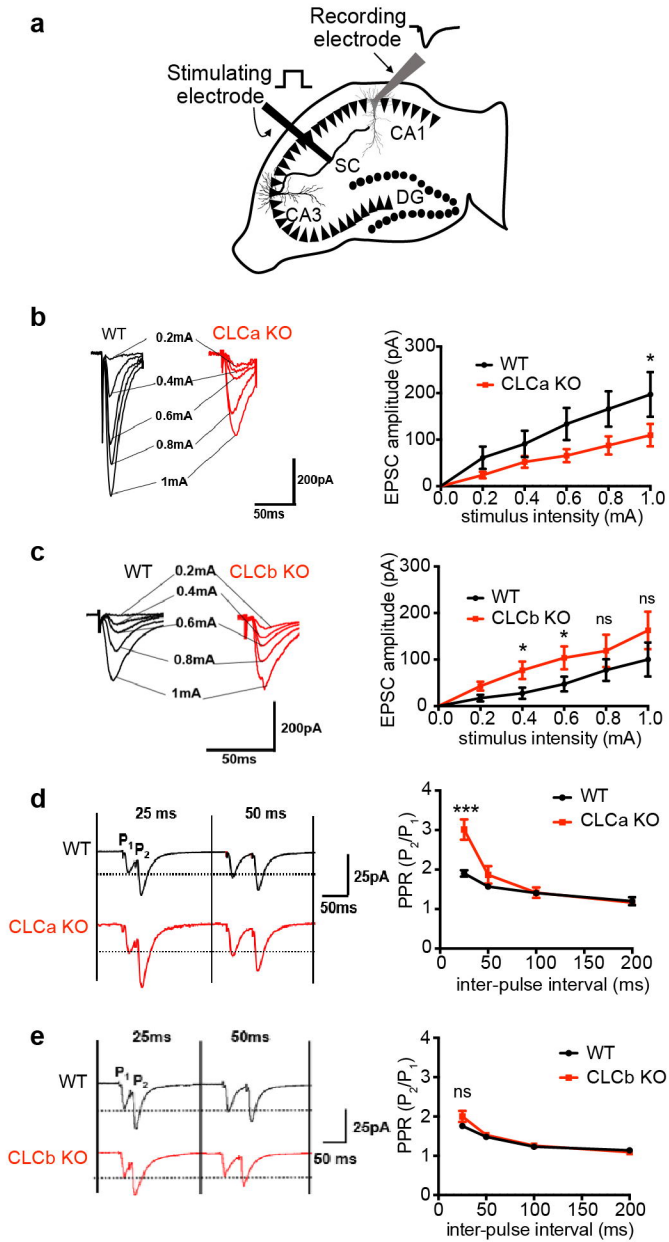


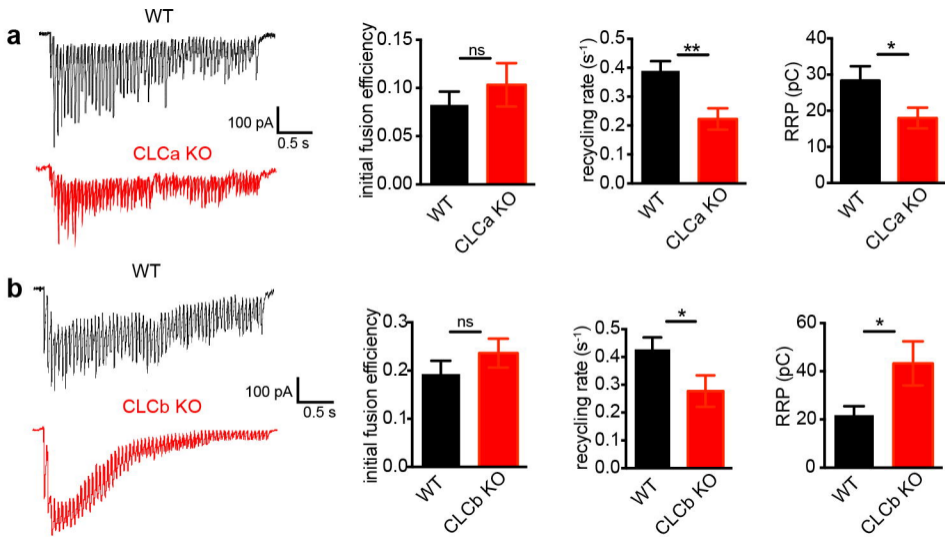
Figure 6

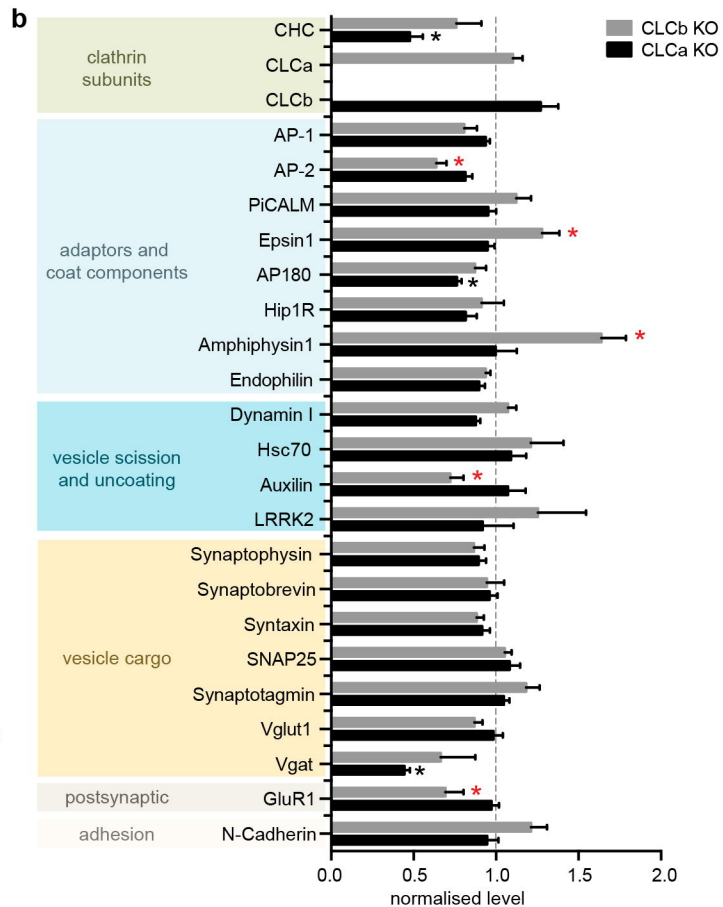
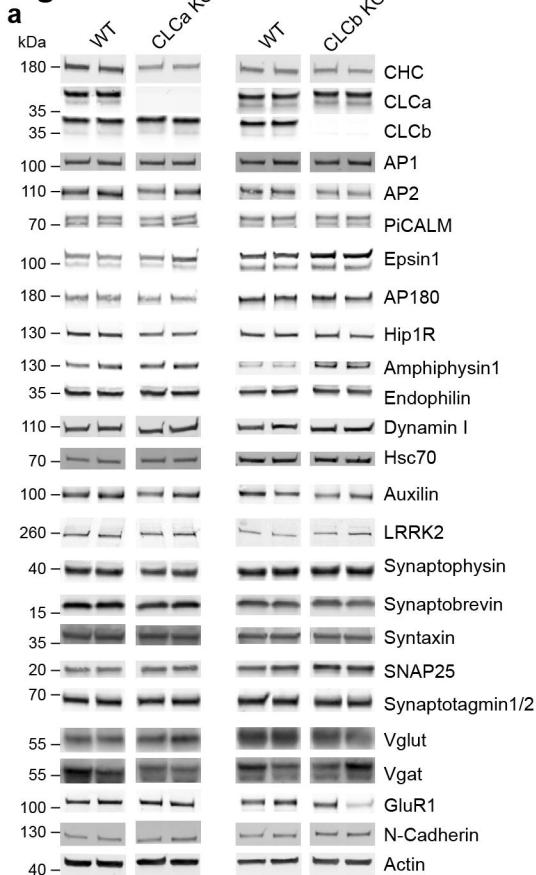
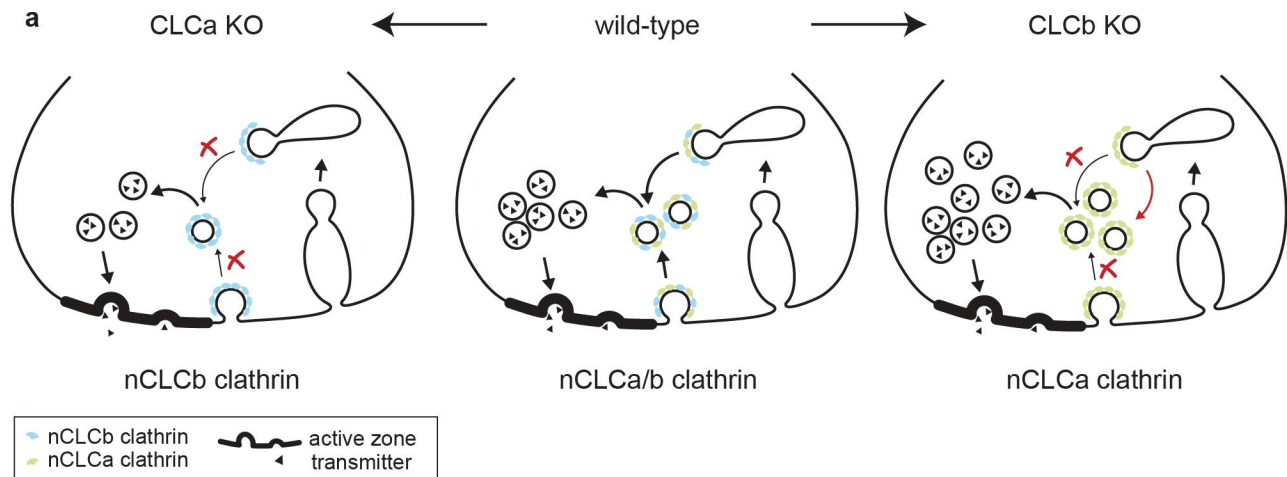
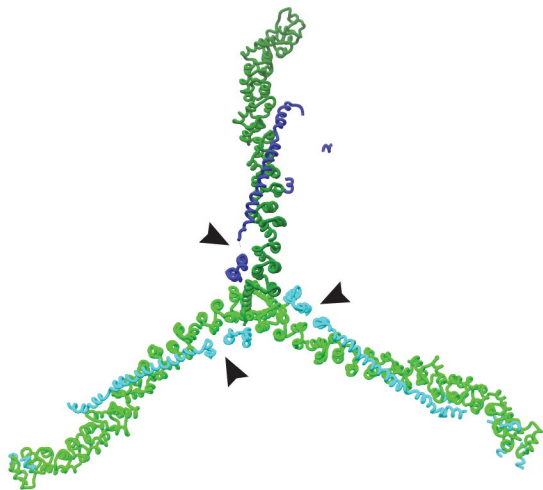
Figure 7

Figure 8**b****c**